Computers and Mathematics with Applications 78 (2019) 1095–1114

Contents lists available at ScienceDirect

Computers and Mathematics with Applications

journal homepage: www.elsevier.com/locate/camwa

An inverse design analysis of mesoscopic implementation of non-uniform forcing in MRT lattice Boltzmann models

Haoda Min [a], Cheng Peng [a], Zhaoli Guo [b], Lian-Ping Wang [a,b,*]

[a] Department of Mechanical Engineering, 126 Spencer Laboratory, University of Delaware, Newark, Delaware 19716-3140, USA

[b] National Laboratory of Coal Combustion, Huazhong University of Science and Technology, Wuhan, PR China

ARTICLE INFO

Article history:
Available online 21 May 2016

Keywords:
Lattice Boltzmann
Non-uniform forcing
MRT
Chapman–Enskog analysis
Inverse design

ABSTRACT

In this paper, the mesoscopic representation of non-uniform forcing is investigated by an inverse design approach, for several MRT (multiple-relaxation-time) lattice Boltzmann models. First, the mesoscopic forcing representation of a standard LBM-MRT model on a square lattice is re-visited. By the multiscale Chapman–Enskog expansion, we derive the most general form of the representation by taking advantage of the MRT formulation. In particular, we show that there are three free components in the mesoscopic representation of forcing. Second, by the same methodology, the forcing scheme of two new rectangular MRT lattice Boltzmann models are derived based on the requirements of the Navier–Stokes equations. These theoretical results are then validated by numerical simulations of a forced Taylor–Green vortex flow, with several different forms of non-uniform forcing to alter the kinetic-energy evolution of the system. The numerical results are in excellent agreement with the corresponding time-dependent analytical solution of flow.

1. Introduction

The lattice Boltzmann equation (LBE) is a fully discrete form in both time and space of the kinetic Boltzmann equation with a finite set of discrete molecular velocities [1,2]. Instead of solving the Navier–Stokes (N–S) equations involving strong nonlinearity at the macroscopic level, the lattice Boltzmann method (LBM) solves the distribution functions that represent the number density of molecules with certain discrete velocities. The distribution functions are updated, typically explicitly, by a quasi-linear collision–propagation process [1–4]. The collision term is simplified by either the use of the single-relaxation-time Bhatnagar–Gross–Krook (BGK) model [3] or the linearized multiple-relaxation-time (MRT) collision model [4,5]. The only nonlinearity occurs in the evaluation of the equilibrium distribution that is used in the collision operator, and this nonlinearity is fully local in the physical space. The macroscopic variables such as pressure, velocity and velocity gradients are then computed as the moments of the distribution functions. Several features of the LBM are highly valued: simplicity of algorithm and implementation, excellent capability of handling complex geometrics [6–8], highly parallelizable since the collision process is completely local and the propagation only involves communication with neighboring nodes [2,3]. With these advantages, the LBM has been developed rapidly in the last several decades and applied extensively for fluid dynamics simulations in many different areas [9–13], particularly multiphase flows or flows with complex boundary [6–8,14].

* Corresponding author at: Department of Mechanical Engineering, 126 Spencer Laboratory, University of Delaware, Newark, Delaware 19716-3140, USA.

E-mail address: lwang@udel.edu (L.-P. Wang).

http://dx.doi.org/10.1016/j.camwa.2016.04.040
0898-1221/

As a mesoscopic method, the LBM has a greater design flexibility than its conventional Computational Fluid Dynamics (CFD) counterparts, and such flexibility is yet to be fully explored. This flexibility originates partially from the fact that the mesoscopic distribution functions contain more information than the few moments governed by the continuity and the N–S equations. Taking advantage of such flexibility, for example, non-uniform forcing and non-standard lattice grids can be incorporated within LBE. Many fluid dynamics problems could involve external forces that are non-uniform and time-dependent, especially in turbulent flows or multiphase flows [6,7,14]. For instance, in the simulation of forced homogeneous turbulence, the turbulent kinetic energy is added into the computational domain with non-uniform time-dependent forcing [6,7]. In the simulation of turbulent flows with dispersed solid particles, the no-slip boundary condition on the particle surface is sometimes converted to a virtual force that is local and non-uniform. Similar situations occur when treating flows with fluid–fluid interfaces. These forces are often formulated at the continuum level, and as such they need to be converted into a mesoscopic form. Whether this conversion is designed appropriately affects the accuracy and consistency of the resulting hydrodynamics. For example, it has been shown that the mesoscopic forcing could affect velocity gradient and strain-rate components calculated from the non-equilibrium moments [15].

It is well known that the N–S equations could be recovered from the lattice Boltzmann equation through several different methods. The first is the Chapman–Enskog (C–E) expansion [1,2]. A multi-scale expansion of Knudsen number is applied in the C–E expansion to derive the compressible Navier–Stokes equations. The second method is the asymptotic analysis [16–18]. In this approach, the Hilbert expansion is used to derive the conserved hydrodynamic variables, and the incompressible N–S equations could be recovered. The third method is the Maxwell iteration [19], in which the time step δ_t is used as the only expansion parameter and the Taylor expansion of distribution function is applied to derive the compressible N–S equations. In this paper, we choose to design the mesoscopic forcing term by using the Chapman–Enskog expansion, in order to explore the impact of the forcing on the hydrodynamic variables and resulting hydrodynamic equations.

Previously, the mesoscopic representation of a forcing term has been widely studied with the BGK collision operators in [20–26]. Advantages and disadvantages of different forcing implementations based on the BGK model have also been compared [26–28]. Through analytically examining the hydrodynamic equations derived from the lattice Boltzmann method with the BGK collision model (LBGK) with different formulations of forcing terms, Guo et al. stated that implementations proposed in [20–24] introduce an additional term $\frac{1}{2}\delta t\nabla\cdot\mathbf{F}$ to the continuity equation affecting the accuracy of simulated hydrodynamics, where δt is the time step size and $\nabla\cdot\mathbf{F}$ is the spatial divergence of the macroscopic force field [26]. Because of the discrete lattice effects, an inappropriate forcing implementation may also contaminate the momentum equations [26]. Guo et al. [26] then derived a mesoscopic forcing, based on a rigorous Chapman–Enskog expansion, that is fully consistent with the N–S equations and maintains the second-order accuracy of the LBM scheme. Guo's forcing scheme has been extended to LBM with the MRT collision operator [15,29]. A D3Q19 MRT LB model with nonuniform forcing was derived by Premnath et al. [29]. Recently, Yong et al. [19] also derived a general representation of the mesoscopic forcing terms of the D2Q9 MRT-LBM using the Maxwell iteration method. As will be shown in this paper, the full flexibility of forcing implementation in the MRT LBM could be developed based on the C–E expansion and the idea of inverse design. Furthermore, all the previous forcing schemes are based on standard lattice grids (square lattice in 2D, cubic lattice in 3D). Recently, LB models using non-standard lattice grids have been successfully developed and validated [30–32], without a systematic analysis of a forcing term. The main objective of this paper is to design the most general formulation of a non-uniform mesoscopic forcing scheme for MRT LBM schemes, on both standard and non-standard lattice grids.

The rest of the paper is arranged as follows. In Section 2, the necessary background of standard MRT LBM will be introduced. The inverse design analysis will be explained in detail by deriving the forcing scheme for the square lattice model. In Section 3 and Appendix, the derivation is repeated for two new MRT LBM models [30,31], using non-standard lattice grids. A modified Taylor–Green vortex flow with non-uniform and time-dependent forcing is introduced in Section 4 to validate the new forcing formulations. Finally, conclusions will be provided in Section 5.

2. An inverse design analysis of MRT-LBM with forcing on a D2Q9 square lattice

In LBM, the domain is decomposed using lattice nodes. For a two dimensional problem, the standard LBM uses a square lattice. In this section, we shall re-visit the forcing formulation of such standard MRT-LBM model for two purposes: first to illustrate the inverse design approach; second to reveal the most general form of mesoscopic forcing implementation.

In LBM, a set of distribution functions f_i are introduced and each evolves in time according to the following equation [4]

$$f_i(\mathbf{x}+\mathbf{e}_i\delta_t, t+\delta_t) - f_i(\mathbf{x}, t) = -\mathbf{M}^{-1}\mathbf{S}\left[\mathbf{m}(\mathbf{x}, t) - \mathbf{m}^{(eq)}(\mathbf{x}, t)\right] + \Phi_i, \tag{1}$$

where the right hand side describes collision interactions and the left hand side provides the exact streaming of the given lattice particle with velocity $\mathbf{e}_i$. For the standard D2Q9 lattice with advective scaling, the 9 particle velocities are: $\mathbf{e}_0 = (0,0)c$, $\mathbf{e}_1 = (1,0)c$, $\mathbf{e}_2 = (0,1)c$, $\mathbf{e}_3 = (-1,0)c$, $\mathbf{e}_4 = (0,-1)c$, $\mathbf{e}_5 = (1,1)c$, $\mathbf{e}_6 = (-1,1)c$, $\mathbf{e}_7 = (-1,-1)c$, and $\mathbf{e}_8 = (1,-1)c$, where $c = \delta_x/\delta_t = 1$ (m s^{-1}) is the lattice velocity unit, δ_x (m) is the lattice spacing and δ_t (s) is the time step size. In Eq. (1), the extra term Φ_i represents the mesoscopic forcing term, which is the main focus of this paper. The components of Φ_i will be designed to reproduce a macroscopic forcing field $\mathbf{F} \equiv (F_x, F_y)$.

Here the MRT collision model is assumed, with the relaxation process applied to the individual moments. The matrix $\mathbf{M}$ transforms the distribution to moments by $\mathbf{m} = \mathbf{M}\mathbf{f}$, with the inverse transform as $\mathbf{f} = \mathbf{M}^{-1}\mathbf{m}$, where $\mathbf{f}$ is a vector containing

f_i. The vector $\mathbf{m}$ contains 9 components derived from the density fluctuation, energy, energy square, momentum in the x direction, energy flux in the x direction, momentum in the y direction, energy flux in the y direction, the normal stress, and the shear stress, in this order, and is written as

$$\mathbf{m} = \left|\delta\rho, e, \varepsilon, j_x, q_x, j_y, q_y, p_{xx}, p_{xy}\right\rangle, \tag{2}$$

where the symbol $|\cdot\rangle$ is a Dirac notation which represents a column vector. Note that, for a nearly incompressible flow, the density is written as $\rho = \rho_0 + \delta\rho$, where ρ_0 is the average density (set to 1) and $\delta\rho$ is the local density fluctuation [2,33]. Based on the isothermal equation of state, the pressure is expressed as $p = \delta\rho c_s^2$ where c_s is the speed of sound. Additionally, the equilibrium moments should have the following form,

$$\mathbf{m}^{(eq)} = \left|\rho^{(eq)}, e^{(eq)}, \varepsilon^{(eq)}, j_x^{(eq)}, q_x^{(eq)}, j_y^{(eq)}, q_y^{(eq)}, p_{xx}^{(eq)}, p_{xy}^{(eq)}\right\rangle. \tag{3}$$

The equilibrium moments $\mathbf{m}^{(eq)}$ must be properly designed to yield the correct hydrodynamic equations. The diagonal relaxation matrix $\mathbf{S}$ specifies the relaxation parameters

$$\mathbf{S} = \mathrm{diag}(s_\rho, s_e, s_\varepsilon, s_j, s_q, s_j, s_q, s_n, s_c), \tag{4}$$

where all non-trivial relaxation parameters should be in the range between 0 and 2. For the standard square lattice, the transform matrix $\mathbf{M}$ is

$$\mathbf{M} = \begin{bmatrix} 1 & 1 & 1 & 1 & 1 & 1 & 1 & 1 & 1 \\ -4 & -1 & -1 & -1 & -1 & 2 & 2 & 2 & 2 \\ 4 & -2 & -2 & -2 & -2 & 1 & 1 & 1 & 1 \\ 0 & 1 & 0 & -1 & 0 & 1 & -1 & -1 & 1 \\ 0 & -2 & 0 & 2 & 0 & 1 & -1 & -1 & 1 \\ 0 & 0 & 1 & 0 & -1 & 1 & 1 & -1 & -1 \\ 0 & 0 & -2 & 0 & 2 & 1 & 1 & -1 & -1 \\ 0 & 1 & -1 & 1 & -1 & 0 & 0 & 0 & 0 \\ 0 & 0 & 0 & 0 & 0 & 1 & -1 & 1 & -1 \end{bmatrix}, \tag{5}$$

where the rows of $\mathbf{M}$ are made to be orthogonal to one another by applying a Gram–Schmidt orthogonalization. The inverse matrix $\mathbf{M^{-1}}$ is just the transpose of $\mathbf{M}$, with a proper normalization for each column of $\mathbf{M^{-1}}$ [4].

The above provides the basic setup of the MRT LBM model on D2Q9 square lattice. The remaining task is to properly formulate $\mathbf{m}^{eq}$ and $\mathbf{\Phi} = \{\Phi_i\}$ in terms of conserved moments and the macroscopic forcing $\mathbf{F}$, such that the Navier–Stokes equations with the forcing $\mathbf{F}$ are properly recovered. Since the Navier–Stokes equations are the moment equations of the distribution function, the most intuitive way to design $\mathbf{m}^{eq}$ and $\mathbf{\Phi}$ is to compare the moment equations from the Chapman–Enskog expansion of the LBE to the Navier–Stokes equations.

The multiscale Chapman–Enskog expansion begins with the Taylor expansion of $f_i(\mathbf{x} + \mathbf{e}_i\delta_t, t + \delta_t)$ in Eq. (1). After multiplying the expanded equation by $\mathbf{M}/\delta_t$, we obtain

$$\left(I\partial_t + \hat{C}_\alpha\nabla_\alpha\right)\mathbf{m} + \frac{\delta_t}{2}\left(I\partial_t + \hat{C}_\alpha\nabla_\alpha\right)^2\mathbf{m} = -\frac{\mathbf{S}}{\delta_t}\left(\mathbf{m} - \mathbf{m}^{(eq)}\right) + \mathbf{\Psi}, \tag{6}$$

where I represents the identity matrix. $\mathbf{\Psi} = \mathbf{M}\mathbf{\Phi}/\delta_t$, ∂_t is the time derivative, ∇_α is the spatial derivatives, $\hat{C}_\alpha = \mathbf{M}\mathrm{diag}(e_{i\alpha})\mathbf{M^{-1}}$. Next, the following standard multiscale expansion is applied to $,\partial_t$, ∇_α and $\mathbf{\Psi}$:

$$\mathbf{m} = \mathbf{m}^{(0)} + \epsilon\,\mathbf{m}^{(1)} + \epsilon^2\mathbf{m}^{(2)} + \cdots, \tag{7a}$$

$$\partial_t = \epsilon\,\partial_{t1} + \epsilon^2\partial_{t2}, \tag{7b}$$

$$\nabla_\alpha = \epsilon\,\nabla_{1\alpha}, \tag{7c}$$

$$\mathbf{\Psi} = \epsilon\,\mathbf{\Psi}^{(1)}, \tag{7d}$$

where ϵ is a small parameter proportional to the Knudsen number. Substituting the multi-scale expansion into Eq. (6) and rearranging the equation according to the order of ϵ, we obtain the following three equations

$$O(1):\ \mathbf{m}^{(0)} = \mathbf{m}^{(eq)}, \tag{8a}$$

$$O(\epsilon):\ \left(I\partial_{t1} + \hat{C}_\alpha\partial_{1\alpha}\right)\mathbf{m}^{(0)} = -\frac{\mathbf{S}}{\delta_t}\mathbf{m}^{(1)} + \mathbf{\Psi}^{(1)}, \tag{8b}$$

$$O(\epsilon^2):\ \partial_{t2}\mathbf{m}^{(0)} + \left(I\partial_{t1} + \hat{C}_\alpha\partial_{1\alpha}\right)\left[\left(I - \frac{\mathbf{S}}{2}\right)\mathbf{m}^{(1)} + \frac{\delta_t}{2}\mathbf{\Psi}^{(1)}\right] = -\frac{\mathbf{S}}{\delta_t}\mathbf{m}^{(2)}. \tag{8c}$$

Each of the equations in Eqs. (8a)–(8c) represents a vector equation of 9 degrees of freedom. According to the ordering of moments as indicated by the transformation matrix $\mathbf{M}$, the 1st, 4th, and 6th of each equation correspond to the governing

equation for mass, and x-momentum, and y-momentum, respectively, with Eq. (8b) relating to the Euler equations and Eq. (8c) to the Navier–Stokes equations.

Since the mass is conserved and the forcing appears at the order ϵ, we have $m_1^{(k)} = 0$ for $k \geq 1$, and $m_{4,6}^{(k)} = 0$ for $k \geq 2$. The first row of Eq. (8b) becomes

$$\partial_{t1} m_1^{(0)} + \partial_{1x} m_4^{(0)} + \partial_{1y} m_6^{(0)} = \Psi_1^{(1)}, \tag{9}$$

which must match with the continuity equation at $\mathcal{O}(\epsilon)$ given by

$$\partial_{t1}\delta\rho + \partial_{1x}(\rho_0 u) + \partial_{1y}(\rho_0 v) = 0. \tag{10}$$

This requires that $m_1^{(0)} = \rho^{(0)} = \delta\rho$, $m_4^{(0)} = j_x^{(0)} = \rho_0 u$, $m_6^{(0)} = j_y^{(0)} = \rho_0 v$ and $\Psi_1^{(1)} = 0$. The 4th and 6th rows of Eq. (8b)

$$\partial_{t1}(\rho_0 u) + \partial_{1x}\left(\frac{2}{3}\delta\rho + \frac{1}{6}e^{(0)} + \frac{1}{2}p_{xx}^{(0)}\right) + \partial_{1y}\left(p_{xy}^{(0)}\right) = -\frac{s_j}{\delta_t} j_x^{(1)} + \Psi_4^{(1)}, \tag{11a}$$

$$\partial_{t1}(\rho_0 v) + \partial_{1y}\left(\frac{2}{3}\delta\rho + \frac{1}{6}e^{(0)} - \frac{1}{2}p_{xx}^{(0)}\right) + \partial_{1x}\left(p_{xy}^{(0)}\right) = -\frac{s_j}{\delta_t} j_y^{(1)} + \Psi_6^{(1)}, \tag{11b}$$

must correspond to the following Euler momentum equations

$$\partial_{t1}(\rho_0 u) + \partial_{1x}\left(p + \rho_0 u^2\right) + \partial_{1y}\left(\rho_0 uv\right) = F_x^{(1)}, \tag{12a}$$

$$\partial_{t1}(\rho_0 v) + \partial_{1y}\left(p + \rho_0 v^2\right) + \partial_{1x}\left(\rho_0 uv\right) = F_y^{(1)}. \tag{12b}$$

Each equation in Eqs. (11) and (12) only contains one time derivative term, one x derivative term and one y derivative term. Therefore, we can match Eq. (11a) with Eq. (12a), and match Eqs. (11b) and (12b) term by term. We then obtain $\frac{2}{3}\delta\rho + \frac{1}{6}e^{(0)} + \frac{1}{2}p_{xx}^{(0)} = p + \rho_0 u^2$, $\frac{2}{3}\delta\rho + \frac{1}{6}e^{(0)} - \frac{1}{2}p_{xx}^{(0)} = p + \rho_0 v^2$ and $p_{xy}^{(0)} = \rho_0 uv$, resulting in $e^{(0)} = (6c_s^2 - 4)\delta\rho + 3\rho_0(u^2 + v^2)$, $p_{xx}^{(0)} = \rho_0(u^2 - v^2)$, and $p_{xy}^{(0)} = \rho_0 uv$. Therefore, 6 equilibrium moments have been determined by matching the Euler equations.

Furthermore, matching the right hand sides of Eqs. (11) and (12), we obtain two constraints

$$-\frac{s_j}{\delta_t} j_x^{(1)} + \Psi_4^{(1)} = F_x^{(1)}, \tag{13a}$$

$$-\frac{s_j}{\delta_t} j_y^{(1)} + \Psi_6^{(1)} = F_y^{(1)}. \tag{13b}$$

From Eq. (8b), we have

$$\mathbf{m}^{(1)} = \delta_t \mathbf{S}^{-1}\left[\mathbf{\Psi}^{(1)} - \left(I\partial_{t1} + \hat{C}_\alpha \partial_{1\alpha}\right)\mathbf{m}^{(0)}\right], \tag{14}$$

which couples the non-equilibrium moment $\mathbf{m}^{(1)}$ to the equilibrium moment $\mathbf{m}^{(0)}$ and the mesoscopic forcing term. Note that S is invertible only when all its diagonal elements are non-zero. Since the relaxation parameters of conserved moments have no impact on the collision term, any non-zero value could be used for the relaxation of conserved moments. Therefore, we could always make the relaxation matrix S to be invertible.

Next, we proceed to the next order, $\mathcal{O}(\epsilon^2)$. First, we define $\mathbf{A}$ as

$$\mathbf{A} = \left(I - \frac{\mathbf{S}}{2}\right)\mathbf{m}^{(1)} + \frac{\delta_t}{2}\mathbf{\Psi}^{(1)}, \tag{15}$$

so that Eq. (8c) becomes

$$O(\epsilon^2) : \partial_{t2}\mathbf{m}^{(0)} + (I\partial_{t1} + \hat{C}_\alpha\partial_{1\alpha})\mathbf{A} = -\frac{\mathbf{S}}{\delta_t}\mathbf{m}^{(2)}. \tag{16}$$

Since $m_1^{(1)} = m_1^{(2)} = \Psi_1^{(1)} = 0$, then A_1 is also equal to zero. The first row of Eq. (16) reads

$$\partial_{t2}\delta\rho + \partial_{1x}A_4 + \partial_{1y}A_6 = 0. \tag{17}$$

This must match the continuity equation at $\mathcal{O}(\epsilon^2)$, namely, $\partial_{t2}\delta\rho = 0$. Therefore, we conclude that $A_4 = A_6 = 0$. Therefore, the following two constraints are obtained

$$A_4 = \left(1 - \frac{s_j}{2}\right) j_x^{(1)} + \frac{\delta_t}{2}\Psi_4^{(1)} = 0, \tag{18a}$$

$$A_6 = \left(1 - \frac{s_j}{2}\right) j_y^{(1)} + \frac{\delta_t}{2}\Psi_6^{(1)} = 0. \tag{18b}$$

Combining Eqs. (13) and (18), we must require that $j_x^{(1)} = -F_x^{(1)}\delta_t/2$, $j_y^{(1)} = -F_y^{(1)}\delta_t/2$, $\Psi_4^{(1)} = (1 - 0.5s_j)F_x^{(1)}$, and $\Psi_6^{(1)} = (1 - 0.5s_j)F_y^{(1)}$.

The next step is to compare the 4th row and 6th row of Eq. (8c) with the Navier–Stokes equations on the order of $\mathcal{O}(\epsilon^2)$, to identify additional constraints. Namely, the two equations

$$\partial_{t2}(\rho_0 u) + \partial_{1x}\left(\frac{A_2}{6} + \frac{A_8}{2}\right) + \partial_{1y}A_9 = 0, \tag{19a}$$

$$\partial_{t2}(\rho_0 v) + \partial_{1y}\left(\frac{A_2}{6} - \frac{A_8}{2}\right) + \partial_{1x}A_9 = 0, \tag{19b}$$

must match the following Navier–Stokes equations at $\mathcal{O}(\epsilon^2)$

$$\partial_{t2}(\rho_0 u) - \partial_{1x}\left[\mu^V\left(\partial_{1x}u + \partial_{1y}v\right) + \mu\left(\partial_{1x}u - \partial_{1y}v\right)\right] - \mu\partial_{1y}\left(\partial_{1y}u + \partial_{1x}v\right) = 0, \tag{20a}$$

$$\partial_{t2}(\rho_0 v) - \partial_{1y}\left[\mu^V\left(\partial_{1x}u + \partial_{1y}v\right) - \mu\left(\partial_{1x}u - \partial_{1y}v\right)\right] - \mu\partial_{1x}\left(\partial_{1y}u + \partial_{1x}v\right) = 0, \tag{20b}$$

where μ and μ^V are the dynamic shear and bulk viscosity, respectively. Comparing Eqs. (19) and (20) yields

$$A_9 = -\mu\left(\partial_{1y}u + \partial_{1x}v\right), \tag{21a}$$

$$A_2 + 3A_8 = -6\left[\mu^V\left(\partial_{1x}u + \partial_{1y}v\right) + \mu\left(\partial_{1x}u - \partial_{1y}v\right)\right], \tag{21b}$$

$$A_2 - 3A_8 = -6\left[\mu^V\left(\partial_{1x}u + \partial_{1y}v\right) - \mu\left(\partial_{1x}u - \partial_{1y}v\right)\right]. \tag{21c}$$

Since A_2, A_8 and A_9 are related to non-equilibrium moments $e^{(1)}$, $p_{xx}^{(1)}$ and $p_{xy}^{(1)}$ and forcing terms $\Psi_2^{(1)}$, $\Psi_8^{(1)}$ and $\Psi_9^{(1)}$ and Eq. (14) states the non-equilibrium moments could be expressed in terms of the forcing term and equilibrium moments, we can obtain three equations that relate $e^{(1)}$, $p_{xx}^{(1)}$, and $p_{xy}^{(1)}$ to $\Psi_2^{(1)}$, $\Psi_8^{(1)}$, and $\Psi_9^{(1)}$ and the viscosity. For example, Eqs. (15) and (21a) together yield

$$\left(1 - \frac{s_c}{2}\right)p_{xy}^{(1)} + \frac{\delta_t}{2}\Psi_9^{(1)} = -\mu\left(\partial_{1y}u + \partial_{1x}v\right). \tag{22}$$

Substituting the expression for $p_{xy}^{(1)}$ from Eq. (14) and setting $s_c' \equiv \left(\frac{1}{s_c} - \frac{1}{2}\right)\delta_t$, we then obtain

$$s_c'\left\{\frac{\Psi_9^{(1)}}{1 - 0.5s_c} - \left(vF_x^{(1)} + uF_y^{(1)}\right) - \frac{1}{3}\left[\partial_{1x}\left(2\rho_0 v + q_y^{(0)}\right) + \partial_{1y}\left(2\rho_0 u + q_x^{(0)}\right)\right]\right\} = -\mu\left(\partial_{1y}u + \partial_{1x}v\right). \tag{23}$$

Recall that the forcing term is introduced to match with the effect of macroscopic force, without affecting other terms in the Navier–Stokes equations. Therefore, in Eq. (23), all terms that are related to the forcing should cancel. This implies that $\Psi_9^{(1)} = (1 - 0.5s_c)(vF_x^{(1)} + uF_y^{(1)})$. Thus, Eq. (23) becomes

$$\frac{s_c'}{3}\left[\partial_{1x}(2\rho_0 v + q_y^{(0)}) + \partial_{1y}(2\rho_0 u + q_x^{(0)})\right] = \mu\left(\partial_{1y}u + \partial_{1x}v\right). \tag{24}$$

To match the form of $\left(\partial_{1y}u + \partial_{1x}v\right)$ on the right hand side of Eq. (24), we must set $q_x^{(0)} = \gamma\rho_0 u$ and $q_y^{(0)} = \gamma\rho_0 v$. Therefore, the shear viscosity must be

$$\mu = \rho_0\frac{s_c'}{3}(2 + \gamma) = \frac{2 + \gamma}{3}\left(\frac{1}{s_c} - \frac{1}{2}\right)\rho_0\delta_t. \tag{25}$$

In a lattice Boltzmann model with the standard lattice, γ is not an adjustable parameter, which we will confirm shortly. However, in the rectangular lattice Boltzmann model, γ can be a free parameter [30,31].

Similarly, by combining the remaining two equations in Eq. (21) with Eqs. (14) and (15), we can determine $\Psi_2^{(1)}$, $\Psi_8^{(1)}$, and an alternative expression for the shear viscosity and an expression for the bulk viscosity based on the requirements of the Navier–Stokes equations. The results are

$$\Psi_2^{(1)} = 6(1 - 0.5s_e)(uF_x^{(1)} + vF_y^{(1)}), \tag{26a}$$

$$\Psi_8^{(1)} = 2(1 - 0.5s_n)(uF_x^{(1)} - vF_y^{(1)}), \tag{26b}$$

$$\mu = \frac{1 - \gamma}{6}\left(\frac{1}{s_c} - \frac{1}{2}\right)\rho_0\delta_t, \tag{26c}$$

$$\mu^V = \frac{(5 - 6c_s^2 + \gamma)}{6}\left(\frac{1}{s_e} - \frac{1}{2}\right)\rho_0\delta_t. \tag{26d}$$

Comparing Eqs. (25) and (26c), we must require $\gamma = -1$ in order for viscosity to be isotropic.

Putting all the above results together for the forcing term, we have

$$\boldsymbol{\Psi} = \epsilon \boldsymbol{\Psi}^{(1)} = \begin{bmatrix} 0 \\ 6(1-0.5s_e)(uF_x + vF_y) \\ \Psi_3 \\ (1-0.5s_j)F_x \\ \Psi_5 \\ (1-0.5s_j)F_y \\ \Psi_7 \\ 2(1-0.5s_n)(uF_x - vF_y) \\ (1-0.5s_c)(vF_x + uF_y) \end{bmatrix}. \tag{27}$$

Several important conclusions can be made: (1) the components of the mesoscopic forcing term are related to the macroscopic forcing F_x and F_y, macroscopic velocity and relaxation times—these forcing terms are added to Eq. (1) as $\boldsymbol{\Phi} = \mathbf{M}^{-1}\boldsymbol{\Psi}$ to realize the effect of macroscopic forcing at the mesoscopic level; (2) since all requirements at the hydrodynamic level have been met, the three undecided forcing components Ψ_3, Ψ_5, and Ψ_7 can be specified *freely*. These elements are associated with energy squared and energy flux in the two spatial directions. The second conclusion regarding the mesoscopic forcing is a reflection of the inherent flexibility in the MRT LBM. This flexibility could be used to potentially improve the numerical stability. (3) The resulting forcing terms derived from the C–E expansion can be compared to Yong et al.'s design [19], which is derived from the Maxwell iteration. The results of the two methods are the same except in Yong et al.'s design, the values of Ψ_3, Ψ_5, and Ψ_7 are determined by the linear stability analysis [4,19].

The equilibrium moments and some important non-equilibrium moments of this model from the above inverse design analysis can now be summarized here:

$$\mathbf{m}^{(0)} = \mathbf{m}^{(eq)} = \begin{bmatrix} \delta\rho \\ \delta\rho\left(6c_s^2 - 4\right) + 3\rho_0\left(u^2+v^2\right) \\ \alpha\delta\rho + \beta\rho_0\left(u^2+v^2\right) \\ \rho_0 u \\ -\rho_0 u \\ \rho_0 v \\ -\rho_0 v \\ \rho_0\left(u^2 - v^2\right) \\ \rho_0 uv \end{bmatrix}. \tag{28}$$

$$\epsilon\mathbf{m}_4^{(1)} = \epsilon j_x^{(1)} = -F_x\delta_t/2, \qquad \epsilon\mathbf{m}_6^{(1)} = \epsilon j_y^{(1)} = -F_y\delta_t/2. \tag{29}$$

The multiscale analysis shows that $m^{(eq)} = m^{(0)}$ and the equilibrium moments are not affected by the forcing. Note that the third equilibrium moment $\varepsilon^{(0)}$ is not restricted in any way by hydrodynamic equations. Thus, two free parameters α and β are introduced here to specify the general form of $\varepsilon^{(0)}$, as assumed in [4]. The above design of equilibrium moments is also identical with the design based on the Maxwell iteration [19].

According to the multi-scale expansion in Eq. (7a), $m_4 \approx m_4^{(0)} + \epsilon\, m_4^{(1)} = \rho_0 u - F_x\delta_t/2$. Therefore, the computation of hydrodynamic variable is affected by the forcing, *i.e.*, $\rho_0 u = m_4 + F_x\delta_t/2$. The same applies to the velocity in the y direction. Namely,

$$u = \left(m_4 + F_x\delta_t/2\right)/\rho_0 = \left(\sum_i f_i e_{ix} + F_x\delta_t/2\right)\Big/\rho_0, \tag{30a}$$

$$v = \left(m_6 + F_y\delta_t/2\right)/\rho_0 = \left(\sum_i f_i e_{iy} + F_y\delta_t/2\right)\Big/\rho_0. \tag{30b}$$

Our derivation shows that $m_1^{(1)} = m_1^{(2)} = \Psi_1^{(1)} = 0$, then the presence of forcing will not affect the local density fluctuation and thus the calculation of pressure will not be affected. The pressure in this model is computed as

$$p = \delta\rho c_s^2 = \sum_i f_i c_s^2. \tag{31}$$

Finally, the shear viscosity and bulk viscosity of this model are determined to be

$$\mu = \frac{\rho_0\delta_t}{3}\left(\frac{1}{s_c} - \frac{1}{2}\right), \tag{32a}$$

$$\mu^V = \frac{(2-3c_s^2)\rho_0\delta_t}{3}\left(\frac{1}{s_e} - \frac{1}{2}\right). \tag{32b}$$

The speed of the sound c_s remains an adjustable parameter, which shows better flexibility of the MRT collision model when compared to the standard BGK model as, for the latter, c_s has to be fixed to $1/\sqrt{3}$.

As proved in [15,30,31], the expression of normal stress and shear stress should be modified if external macroscopic forces are introduced. In this paper, the expression of normal stress and shear stress of the square lattice model could be derived from Eq. (21):

$$\tau_{xx} = -\tau_{yy} = -\frac{1}{2}\left[\left(1-\frac{s_n}{2}\right)\epsilon m_8^{(1)} + \frac{\delta_t}{2}\Psi_8\right], \tag{33a}$$

$$\tau_{xy} = -\left(1-\frac{s_c}{2}\right)\epsilon m_9^{(1)} - \frac{\delta_t}{2}\Psi_9, \tag{33b}$$

where $\epsilon m_8^{(1)}$ and $\epsilon m_9^{(1)}$ are calculated according to $\epsilon\mathbf{m}^{(1)} = -\mathbf{m}^{(0)} = \mathbf{Mf} - \mathbf{m}^{(0)}$ and $\mathbf{m}^{(0)}$ comes from Eq. (28). Ψ_8 and Ψ_9 should be calculated based on Eq. (27). Thus, the effect of forcing is included when calculating normal stress, shear stress (or strain tensor and velocity gradients).

In summary, for this D2Q9 square lattice model, the mesoscopic forcing scheme, equilibrium moments, and other information including the expression of viscosity, normal and shear stress, *etc.* have been designed based on an inverse design analysis. The result provides the most general formulation of the mesoscopic forcing. Specifically, we conclude that three components of the mesoscopic forcing can be left as free parameters as they have no bearing on the Navier–Stokes equations. In addition, the resulting mesoscopic forcing is the same as those in Yong et al.'s model [19] based on the Maxwell iteration [4,19]. In the next section, we will apply the inverse design analysis to recently developed new models using a non-standard lattice grid.

3. Inverse design of MRT-LBM with forcing on rectangular lattice grids

The analysis in the previous section illustrates that, in principle, the mesoscopic forcing term can be designed for any LBM model using the Chapman–Enskog analysis and the requirements of hydrodynamic equations. In this section, we will use the same inverse analysis to design the forcing scheme of one recently developed MRT-LBM models for non-standard, rectangular lattice.

Non-standard lattice models are desired because the computational efficiency could be greatly improved by using these models for non-isotropic flows. For example, when simulating turbulent flows in a long channel or a long pipe, the flow properties in the streamwise direction vary more gradually than those in the wall normal direction. Non-standard lattice based on a rectangular or cuboid grid is then more appropriate.

In this paper, we consider two rectangular MRT LB models with a rectangular lattice. The forcing scheme based on Zong et al.'s model [30], namely, the θ model, will be derived in this section. The forcing scheme based on Peng et al.'s model [31], namely, the extended equilibrium model, is presented in the Appendix.

Previously, two rectangular models have already been developed by Bouzidi et al. [34] and Zhou [35], respectively. However, Zong et al. [30] and Peng et al. [31] showed that the viscosity in these two models is anisotropic, namely, the effective viscosity in one spatial direction is different from the other direction, resulting from the use of anisotropic lattice grid. In a two dimensional rectangular model, there could be three shear viscosities ν, ν_x, ν_y and two bulk viscosities ν_x^V, ν_y^V associated with transport of different stress components in different spatial directions, derivable from the Chapman–Enskog expansion. In order to achieve the full isotropy, three additional constraints must be imposed in order to satisfy the following three relations

$$\nu = \nu_x = \nu_y, \tag{34a}$$

$$\nu_x^V = \nu_y^V. \tag{34b}$$

In Bouzidi et al.'s model, only two constraints (a relation between s_n and s_c, and a second relation between s_e and s_c) are available, which are not sufficient. In the θ model [30], a new degree of freedom θ is introduced to re-arrange the two moments (*i.e.*, the energy and normal-stress) in the transformed phase space. Consequently, a third constraint on the θ variable was imposed to fully restore the isotropy condition.

An alternative solution is suggested by Peng et al. [31], who included stress components into equilibrium moments of energy, normal, and shear stress in order to restore the isotropy. In total there are 5 new parameters, *i.e.*, two in the equilibrium energy moment, two in equilibrium normal-stress moment, and one in equilibrium shear-stress moment, leading to 5 additional degrees of freedom. Three of them are used to satisfy the three relations in Eq. (34), while the remaining two act to adjust the shear and bulk viscosities independent of the relevant relaxation parameters.

For a D2Q9 MRT LB model on a rectangular lattice, the distribution is still governed by Eq. (1). $\mathbf{\Phi}$ on the right hand side is the mesoscopic forcing term which is used to represent the effect of the macroscopic forcing at the mesoscopic level. The transformation from $\mathbf{f}$ to $\mathbf{m} = \mathbf{Mf}$ is formally the same, and the relaxation matrix remains a diagonal matrix. Therefore, by applying the Chapman–Enskog expansion to Eq. (1), the expanded equations should be in the same form as Eq. (8).

However, the transform matrix is different from the one for the square lattice because different discrete velocities are applied in different directions according to $\mathbf{e}_0 = (0,0)c$, $\mathbf{e}_1 = (1,0)c$, $\mathbf{e}_2 = (0,a)c$, $\mathbf{e}_3 = (-1,0)c$, $\mathbf{e}_4 = (0,-a)c$, $\mathbf{e}_5 = (1,a)c$, $\mathbf{e}_6 = (-1,a)c$, $\mathbf{e}_7 = (-1,-a)c$, and $\mathbf{e}_8 = (1,-a)c$, where $a = dy/dx$ is the lattice aspect ratio, dx and dy are lattice spacing in the x- and y-direction, respectively. $c = dx/\delta_t = 1$ (m s^{-1}) is the lattice velocity unit and δ_t (s) is the time step size. Thus in Eq. (8), $\hat{C}_\alpha = \mathbf{M}\mathrm{diag}(e_{i\alpha})\mathbf{M^{-1}}$ in the rectangular model is different from the one in the square model.

Specifically, in Zong et al.'s model, an additional parameter θ is introduced to couple the energy moment and normal stress moment [30], introduced initially by Bouzidi et al. [34], denoted as e^B and p^B_{xx}, respectively. Namely, these two moments are modified as

$$e = e^B + \theta p^B_{xx}, \tag{35a}$$

$$p_{xx} = p^B_{xx} - \theta e^B. \tag{35b}$$

Therefore, the parameter θ could be viewed as a coupling coefficient used to re-arrange the two-dimensional moment sub-space. The above transformation amounts to a rotation in the two-dimensional moment sub-space, namely, $\theta \sim \tan\phi$, where ϕ is the rotation angle. This transform preserves the orthogonality property of all moments. Therefore, the moment transformation matrix in Zong et al.'s model becomes [30]:

$$\mathbf{M} = \begin{bmatrix} 1 & 1 & 1 & 1 & 1 & 1 & 1 & 1 & 1 \\ -2R_1 & R_2 & R_3 & R_2 & R_3 & R_1 & R_1 & R_1 & R_1 \\ 4 & -2 & -2 & -2 & -2 & 1 & 1 & 1 & 1 \\ 0 & 1 & 0 & -1 & 0 & 1 & -1 & -1 & 1 \\ 0 & -2 & 0 & 2 & 0 & 1 & -1 & -1 & 1 \\ 0 & 0 & a & 0 & -a & a & a & -a & -a \\ 0 & 0 & -2a & 0 & 2a & a & a & -a & -a \\ -2R_4 & R_5 & R_6 & R_5 & R_6 & R_4 & R_4 & R_4 & R_4 \\ 0 & 0 & 0 & 0 & 0 & a & -a & a & -a \end{bmatrix}, \tag{36}$$

where $R_1 = (a^2+1) + \theta(a^2-1)$, $R_2 = (1-2a^2) + \theta(a^2+2)$, $R_3 = (a^2-2) - \theta(1+2a^2)$, $R_4 = (a^2-1) - \theta(a^2+1)$, $R_5 = (a^2+2) - \theta(1-2a^2)$, and $R_6 = -(2a^2+1) - \theta(a^2-2)$.

By applying the same inverse design analysis, the following forcing scheme can be derived:

$$\mathbf{\Psi} = \begin{bmatrix} 0 \\ 6\left(1-0.5s_e\right)\left[\left(a^2\theta+1\right)uF_x + \left(1-\dfrac{\theta}{a^2}\right)vF_y\right] \\ \Psi_3 \\ \left(1-0.5s_j\right)F_x \\ \Psi_5 \\ \left(1-0.5s_j\right)F_y \\ \Psi_7 \\ 6(1-0.5s_n)\left[\left(a^2-\theta\right)uF_x - \left(\theta+\dfrac{1}{a^2}\right)vF_y\right] \\ \left(1-0.5s_c\right)\left(vF_x+uF_y\right) \end{bmatrix}. \tag{37}$$

The above mesoscopic forcing formulation is formally similar to the forcing scheme for a square lattice model derived in Section 2, Eq. (27). A few differences are noted here. First, the coefficient in the front of Ψ_8 is 6 in the rectangular model and it is 2 in the square model. This is because the normal stress moment p_{xx} in the rectangular model is multiplied by a factor 3 during the Gram–Schmidt orthogonalization to simplify the calculation and the transformation matrix. Second, in the rectangular model, only Ψ_2 and Ψ_8 are affected by the additional parameter θ. This is also reasonable because θ is a coupling coefficient between the second moment and the eighth moment in the standard model. It is noted that Eq. (37) reduces to Eq. (27), when $a \to 1$ and $\theta \to 0$.

Similar to the case of square lattice, there are three free forcing terms in the rectangular model: Ψ_3, Ψ_5 and Ψ_7. Their values have no impact on the Navier–Stokes equations so they can be chosen arbitrarily as long as the model is numerically stable.

The equilibrium moments of the rectangular model have been determined to take the form, using the density splitting $\rho = \rho_0 + \delta\rho$ as in Section 2,

$$\mathbf{m}^{(\mathbf{0})} = \mathbf{m}^{(\mathbf{eq})} = \begin{bmatrix} \delta\rho \\ 2\left(3c_s^2 - r_1\right)\delta\rho + 3\rho_0\left(u^2+v^2\right) + \theta\left[\left(3r_3c_s^2 - 2r_2\right)\delta\rho + 3\rho_0\left(a^2u^2 - \dfrac{v^2}{a^2}\right)\right] \\ \alpha\delta\rho + \beta\rho_0(u^2+v^2) \\ \rho_0 u \\ \dfrac{\gamma - 2r_2}{a^2}\rho_0 u \\ \rho_0 v \\ \gamma\rho_0 v \\ \left(3r_3c_s^2 - 2r_2\right)\delta\rho + 3\rho_0\left(a^2u^2 - \dfrac{v^2}{a^2}\right) - \theta\left[2\left(3c_s^2 - r_1\right)\delta\rho + 3\rho_0(u^2+v^2)\right] \\ \rho_0 uv \end{bmatrix}, \tag{38}$$

where $r_1 = a^2+1, r_2 = a^2-1, r_3 = \frac{a^4-1}{a^2}$ and $r_4 = \frac{a^4+1}{a^2}$. As indicated in Section 2, γ is the coefficient of equilibrium moment $q_y^{(eq,0)}$ and it has the same definition as what is defined in Section 2 for the square lattice model. In the square lattice model, γ has to be -1, as indicated by Eqs. (25) and (26c). However, γ is a free parameter here and it could be used to improve the numerical stability of the model. The above equilibrium moments are identical to the design in Zong et al. [30], who derived their model without considering the forcing term. Therefore, this is a further confirmation that the equilibrium moments are not affected by the forcing. However, the form of non-equilibrium moments must be modified due to the presence of forcing. As shown in Section 2 and in [15,30,31], the expressions of normal stress and shear stress must also be modified. For example, the stress components should now be computed as

$$\tau_{xx} = -\tau_{yy} = -\frac{\left(d_1 - a^2 d_2\right)\left[(1-0.5s_e)\,\epsilon m_2^{(1)} + 0.5\delta_t \Psi_2\right] + \left(a^2 d_1 + d_2\right)\left[(1-0.5s_n)\,\epsilon m_8^{(1)} + 0.5\delta_t \Psi_8\right]}{6 d_3 d_4}, \tag{39a}$$

$$\tau_{xy} = -\left(1-0.5s_c\right)\epsilon m_9^{(1)} - 0.5\delta_t \Psi_9, \tag{39b}$$

where $d_1 = a^2\theta + 1$, $d_2 = a^2 - \theta$, $d_3 = a^4 + 1$, $d_4 = \theta^2 + 1$. $\epsilon m_2^{(1)}$, $\epsilon m_8^{(1)}$, and $\epsilon m_9^{(1)}$ are calculated according to $\epsilon \mathbf{m}^{(1)} = -\mathbf{m}^{(0)} = \mathbf{Mf} - \mathbf{m}^{(0)}$ and $\mathbf{m}^{(0)}$ is provided by Eq. (38). Ψ_2, Ψ_8 and Ψ_9 should be calculated based on Eq. (37). Thus, the effect of forcing enters the computation of the normal stress and shear stress (or strain-rate components). For the rectangular lattice, the relations given by Eqs. (30) and (31) can still be used to compute the macroscopic velocity and pressure from the moments.

4. Numerical validations

The inverse design ensures that the three derived forcing schemes (one for the square lattice, two for the rectangular lattice) are consistent with the Navier–Stokes equations. In this section, they will be validated against analytical solutions of an altered 2D forced Taylor–Green vortex flow, under a non-uniform forcing.

4.1. The forced 2D Taylor–Green vortex

In order to validate the forcing schemes, a 2D forced Taylor–Green vortex flow is designed. Namely, an external non-uniform body force is applied to drive the two-dimensional Taylor–Green vortex flow, to either cause a more rapid decay or even growth of flow velocity magnitude. The external body force is both non-uniform and time-dependent, yet an analytical solution can be obtained for the flow. Therefore, this specially designed flow provides a very rigorous test of the mesoscopic forcing formulation.

In the standard Taylor–Green vortex flow, no external force is applied so the flow decays monotonically in time. The physical domain of this problem is: $(x, y) \in (0 : L_x, 0 : L_y)$ with periodic boundary conditions applied in each direction. We set $L_x = L_y = L$. The velocity and pressure of the flow can be expressed analytically by

$$u(x, y, t) = -U_0 \cos\left(\frac{2\pi x}{L}\right)\sin\left(\frac{2\pi y}{L}\right) e^{-\frac{8\pi^2 \nu t}{L^2}}, \tag{40a}$$

$$v(x, y, t) = U_0 \sin\left(\frac{2\pi x}{L}\right)\cos\left(\frac{2\pi y}{L}\right) e^{-\frac{8\pi^2 \nu t}{L^2}}, \tag{40b}$$

$$p(x, y, t) = -\frac{1}{2}\rho_0 U_0^2 \cos\left[\frac{2\pi}{L}(x-y)\right]\cos\left[\frac{2\pi}{L}(x+y)\right] e^{-\frac{16\pi^2 \nu t}{L^2}} + P_0, \tag{40c}$$

where U_0 is a characteristic velocity of the Taylor–Green flow, P_0 is a background pressure which could be chosen arbitrarily, ν is the kinematic viscosity, and t is the time. This flow is divergence-free and satisfies the two-dimensional incompressible Navier–Stokes equations

$$\frac{\partial \mathbf{u}}{\partial t} + \mathbf{u}\cdot\nabla\mathbf{u} = -\frac{\nabla p}{\rho} + \nu\nabla^2\mathbf{u} + \mathbf{F}, \tag{41}$$

with $\mathbf{F} = (0, 0)$.

In absence of external forcing, a careful examination of the analytical solution Eq. (40) indicates that the advection term is in fact completely balanced by the pressure gradient term, and the time derivative term is identical to the viscous term. A non-zero external force $\mathbf{F}$ added to the N–S equations will alter the time evolution of velocity and pressure. However, assuming the same spatial dependence of the velocity field and $\mathbf{F}$, the balance between advection and pressure gradient terms can be still maintained. The N–S equations can be then partitioned into two parts, as

$$\frac{\partial \mathbf{u}}{\partial t} = \nu\nabla^2\mathbf{u} + \mathbf{F}, \quad \text{with } \mathbf{u}\cdot\nabla\mathbf{u} = -\frac{\nabla p}{\rho}. \tag{42}$$

Table 1
Physical parameters used for the forced Taylor–Green vortex flow.

Cases	Model	a	L	$n_x \times n_y$	U_0	P_0	ν	Re_0
1	Square	1	200	200×200	0.05	0	0.1	100
2	Zong et al.	0.8	200	200×250	0.05	0	0.1	100
3	Zong et al.	0.4	200	200×500	0.025	0	0.05	100
4	Peng et al.	0.8	200	200×250	0.1	0	0.2	100
5	Peng et al.	0.5	200	200×400	0.05	0	0.1	100

Table 2
Input parameters in the MRT-LBM schemes used for the forced Taylor–Green vortex flow. Note that the case numbers correspond to those in Table 1.

Cases	γ	c_s^2	s_e	s_n	s_e
1	-1	0.3333	1.200	1.250	1.250
2	-1.15	0.3333	1.888	1.067	1.172
3	-1.75	0.09	1.681	0.570	0.909
4	-1	0.3333	1.786	0.684	0.909
5	-1.5	0.16	1.748	0.531	0.909

By setting $\mathbf{F} = \frac{8\pi^2\nu}{L^2}(1-Q)\mathbf{u}$, the new analytical solution of the flow evolution is

$$u(x,y,t) = -U_0 \cos\left(\frac{2\pi x}{L}\right) \sin\left(\frac{2\pi y}{L}\right) e^{-\frac{8\pi^2\nu t}{L^2}Q}, \tag{43a}$$

$$v(x,y,t) = U_0 \sin\left(\frac{2\pi x}{L}\right) \cos\left(\frac{2\pi y}{L}\right) e^{-\frac{8\pi^2\nu t}{L^2}Q}, \tag{43b}$$

$$p(x,y,t) = -\frac{1}{2}\rho_0 U_0^2 \cos\left[\frac{2\pi}{L}(x-y)\right] \cos\left[\frac{2\pi}{L}(x+y)\right] e^{-\frac{16\pi^2\nu t}{L^2}Q} + P_0, \tag{43c}$$

$$\tau_{xx}(x,y,t) = -\tau_{yy}(x,y,t) = \frac{4\pi\rho_0 U_0 \nu}{L} \sin\left(\frac{2\pi x}{L}\right) \sin\left(\frac{2\pi y}{L}\right) e^{-\frac{8\pi^2\nu t}{L^2}Q}, \tag{43d}$$

where τ_{xx} is the theoretical normal stress component of the flow. The shear stress remains identically zero at all times. Note that the stress evolution and profiles are rarely examined in other studies, but they are very important in identifying any defect in an MRT-LBM model, as demonstrated in [30,31]. It follows that the flow evolution can be manipulated by choosing different Q values:

1. When $Q = 1$, there is no external force applied so the standard analytical solution Eq. (40) is recovered.
2. When $Q = 0.5$, the exponential decay rate is half of the original decay rate because the external body force injects the kinetic energy into the flow.
3. When $Q = 0$, the decay rate is zero so all hydrodynamic variables become independent of time. In this case, the forcing term and the viscous dissipation term are balanced.
4. When $Q = -0.5$, the magnitudes of velocity and pressure actually grow with time, as more kinetic energy is added than the dissipation by the viscous term.

Therefore, the parameter Q sets *decaying or growth rate* of this forced Taylor–Green vortex flow.

4.2. Parameter settings

Before we present the simulation results, the parameter settings of the three models, *i.e.,* the standard MRT model on square lattice and two MRT models on rectangular lattice, should be introduced. According to our analysis in Sections 2 and 3, the common key input parameters in all three models are: the aspect ratio a, the speed of sound c_s, the coefficient in the equilibrium energy flux γ, shear viscosity ν, and the relaxation matrix $\mathbf{S}$ as given by Eq. (4). The physical parameters in the forced Taylor–Green vortex flow should also be defined: the characteristic velocity U_0, the background pressure P_0, the domain size L, the initial Reynolds number Re_0, and the decay rate parameter Q. These input parameters are listed in Tables 1 and 2. Note that Cases 2 and 3 use Zong et al.'s LBM MRT scheme [30] while Cases 4 and 5 are based on Peng et al.'s LBM MRT scheme [31].

As presented in the tables, two different aspect ratios are tested for each rectangular model, and a total of 5 cases are considered. For each case, 3 different values of Q are tested. For all cases, the initial flow Reynolds number Re_0 is set to 100, the background pressure P_0 is zero, and the domain size is 200 lattice grids in the x direction. Since the initial Reynolds number and the domain size are constant, the shear viscosity and the characteristic velocity U_0 are linearly related. Once U_0

is specified, ν is also determined. The average density ρ_0 is set to 1 so the value of kinematic viscosity ν is identical to that of the dynamic viscosity μ. Thus in the square model (case 1), the relaxation time s_c can be determined according to Eq. (26). In square lattice model, we usually pre-define the relaxation time s_e instead of bulk viscosity. Therefore, in case 1, we choose $s_e = 1.2$ and the bulk viscosity is then calculated inversely through Eq. (26). In Cases 2 and 3 (based on Zong et al.'s model), s_c can still be calculated by Eq. (32). The values of s_e and s_n are then decided by s_c because these two relaxation times are used to restore the isotropy of viscosity in Zong et al.'s model, and thus they must be related to s_c (*i.e.,* Eqs. (49a,b) in [30]). In Cases 4 and 5 based on Peng et al.'s model [31], although the two relaxation times, s_e and s_n, can be chosen arbitrarily between 0 and 2 in principle due to the sufficient degrees of freedom introduced in this model, for fair comparisons, here we still applied the same relations as in Zong et al.'s model to specify s_n and s_e in terms of s_c and other parameters. In other words, for the validation here, we do not utilize all the freedom in Peng et al.'s model. Other relaxation times listed in Eq. (4) are not directly relevant to the hydrodynamic equations, we set them to 1.2 for simplicity. Alternatively, their values could be optimized based on a linear stability analysis [34]. In-depth discussions on how to choose γ and c_s^2 are provided in [30,31], so they are not repeated here.

The initial equilibrium and non-equilibrium moments may be calculated from the analytical solution of hydrodynamics (velocity, pressure, velocity gradient), based on the Chapman–Enskog analysis. Then, the initial distribution functions are determined by summing the equilibrium and non-equilibrium moments. Finally, it has been shown in Sections 2 and 3 that in each model there are 3 undecided mesoscopic forcing terms. They are simply set to zero in this study.

4.3. Results

The simulation results are now presented. First, the time evolutions of velocity, pressure, and normal stress at a given point are displayed for all three models, along with their theoretical solutions. In Case 1, the location $(x/L, y/L) = (0.1225, 0.2475)$ is chosen as all hydrodynamic variables at this point are non-trivial. In Case 3, the location $(x/L, y/L) = (0.1225, 0.248)$ is chosen and in Case 5, $(x/L, y/L) = (0.1225, 0.24875)$ is chosen. The physical position of these points in different models are close to each other. However, due to the variation of lattice size, it is not possible to make the physical position in different models identical in the y direction unless numerical interpolation is used.

The simulation results of Case 1 are shown in Fig. 1. Each sub-plot has 6 lines with 3 different colors. Solid lines are simulation results and dash lines are theoretical results. Different colors represent different Q values. All results are in excellent agreement with the analytical solutions calculated from Eqs. (43). When $Q = 0.5$, the velocity, pressure and normal stress are decaying exponentially with half of the exponential decay rate of the original Taylor–Green vortex. When $Q = 0$, the energy that is injected into the flow is the same as the dissipation so the velocity, pressure and stress are always a constant. When $Q = -0.5$, the energy supplied is larger than the viscous dissipation so the magnitudes of all hydrodynamic variables grow exponentially.

In Fig. 2, the left column displays the results for Case 3 at $(x/L, y/L) = (0.1225, 0.248)$. The right column of Fig. 2 shows the results for Case 5 at $(x/L, y/L) = (0.1225, 0.24875)$. All results are in excellent agreement with the theoretical results. Figs. 1 and 2 also demonstrate how the Q value affect the flow evolution and this is captured precisely by the forcing formulation.

Next, we shall compare profiles of hydrodynamic variables on a vertical line at $x/L = 0.125$, at $tU_0/L = 1$. This line passes through the point where the time evolutions were shown above.

Fig. 3 shows the profiles for velocity, pressure and normal stress for Case 1. Again, each sub-plot has 6 different lines. Three dash lines are results with different decay parameters Q (and thus forcing magnitudes). Three solid lines show the corresponding theoretical results calculated from Eqs. (43). Different colors correspond to different forcing magnitudes or decay rates of the flow. Large positive Q value results in faster decay of flow energy. Therefore, the magnitude of any hydrodynamic quantity is smaller for larger Q, which is exactly the case as shown in Fig. 3. In all cases, the numerical results are identical to the theoretical solution. The results confirm the more general design of the mesoscopic forcing for the square lattice.

The forcing formulations for Zong et al.'s [30] and Peng et al.'s [31] models on a rectangular lattice are validated by results of velocity, pressure, and stress profiles in Fig. 4. The left column of Fig. 4 displays results of Case 3 at $x/L = 0.125$. The right column of Fig. 4 shows results of Case 5. All results are at $tU_0/L = 1$, and three different Q values are tested for each case. By comparing Fig. 4 with Fig. 3, we confirm that the hydrodynamic results from all three different models are identical. Unlike the results of one-point time evolutions, the physical position of the vertical lines can be made identical for the three MRT LBM models as the lattice has the identical spacing in the x direction.

Therefore, we could directly compare the results of all 5 cases shown in Tables 1 and 2, which is done in Fig. 5, for both velocity components, pressure, and the normal stress on the vertical line at $x/L = 0.125$. For this plot, Q is set to 0.5. The theoretical solutions are also presented as black lines. There are two groups of data in Fig. 5(c) and (d), one for $tU_0/L = 5/16$, the other for $tU_0/L = 7/8$. Clearly, all results from different models are identical and all of them are consistent with the corresponding theoretical results.

It has been proved that the lattice Boltzmann method has a second-order accuracy in space [20,31,30]. The order of accuracy of three models and their forcing schemes in this paper are also checked by using the 2D forced Taylor–Green vortex. For all three models (one square model and two rectangular models) tested, some key parameters are listed in Table 3:

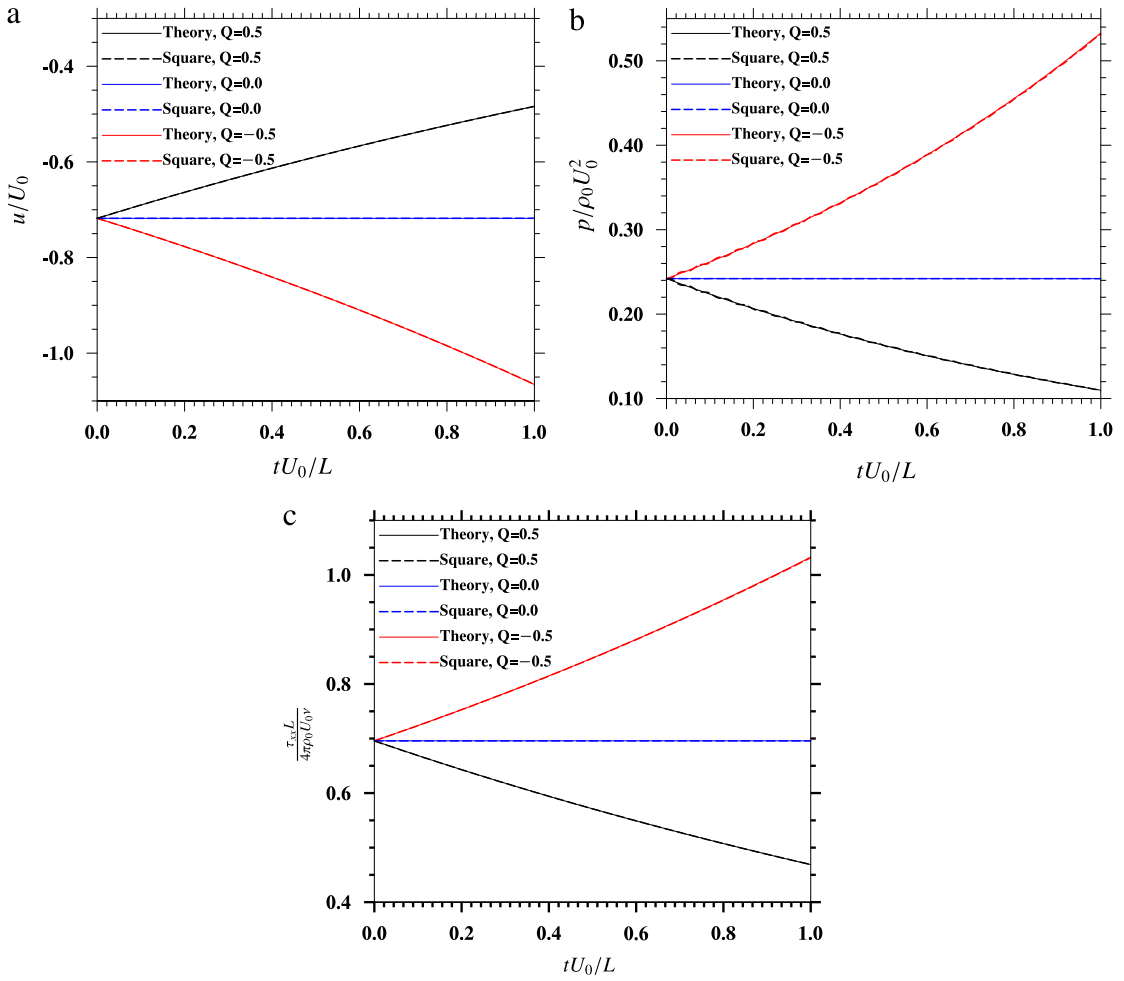

Fig. 1. The time evolutions of hydrodynamic variables at $(x/L, y/L) = (0.1225, 0.2475)$. Results come from case 1 in Tables 1 and 2, and the theoretical solutions given by Eq. (43). (a) Velocity in the x direction: u; (b) Pressure: p; (c) Normal stress: τ_{xx}. All quantities are normalized as indicated. (For interpretation of the references to color in this figure legend, the reader is referred to the web version of this article.)

Table 3
Physical parameters used to check the order of accuracy.

Cases	Model	a	P_0	ν	Re_0	γ	c_s^2	s_e	s_n	s_e
1	Square	1	0	0.1	10	−1	0.3333	1.200	1.250	1.250
2	Zong et al.	0.4	0	0.1	10	−1.75	0.09	1.681	0.570	0.909
3	Peng et al.	0.5	0	0.1	10	−1.5	0.16	1.748	0.531	0.909

In order to measure the order of accuracy, the $L1$ and $L2$ errors are calculated as

$$\epsilon_{L1}(t) = \frac{\sum_{x,y} |q_n(x,y,t) - q_t(x,y,t)|}{\sum_{x,y} |q_t(x,y,t)|}, \tag{44a}$$

$$\epsilon_{L2}(t) = \frac{\sqrt{\sum_{x,y} |q_n(x,y,t) - q_t(x,y,t)|^2}}{\sqrt{\sum_{x,y} |q_t(x,y,t)|^2}}, \tag{44b}$$

where $q_n(x, y, t)$ and $q_t(x, y, t)$ represent the numerical value and corresponding theoretical value of a quantity at location (x, y) and time t. We verified the order of accuracy for velocity $\mathbf{u}$, and the normal stress τ_{xx}. Results are shown in Tables 4–6.

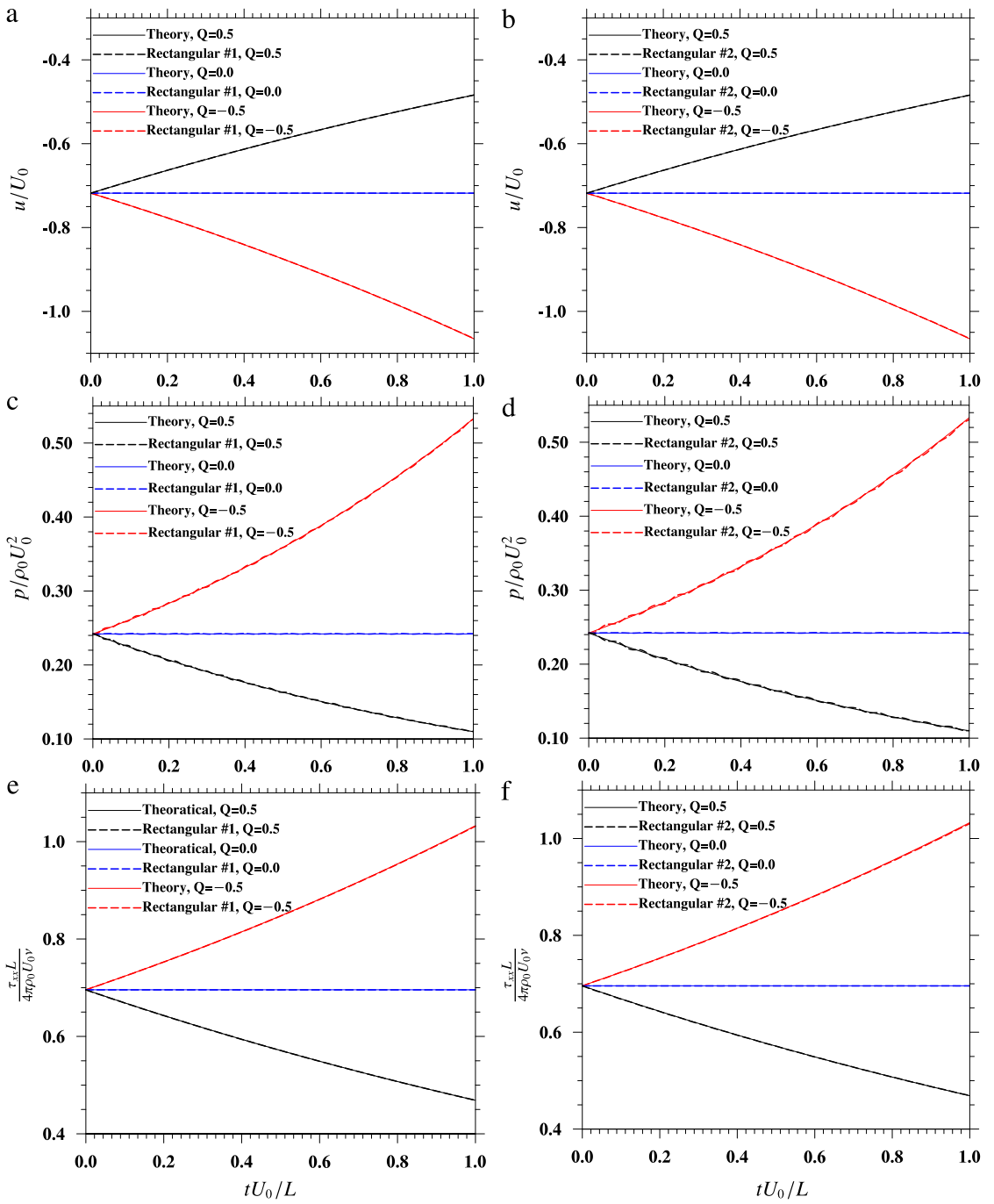

Fig. 2. The time evolutions of hydrodynamic variables at $(x/L, y/L) = (0.1225, 0.248)$. Results come from case 3 in Tables 1 and 2, and the theoretical solutions given by Eq. (43). (a) Velocity in the x direction: u; (c) Pressure: p; (e) Normal stress component: τ_{xx}. The corresponding results for Case 5 are shown in (b), (d), and (f), at $(x/L, y/L) = (0.1225, 0.24875)$. All quantities are normalized as indicated.

For each model, the $L1$ and $L2$ error norms for velocity and normal stress at different grid resolutions are calculated according to Eq. (44). The order of accuracy could be estimated based on either $L1$ or $L2$ error norm. Assume the error norm calculated from one given resolution is $\epsilon_0(t)$, as we increase the resolution by a factor of m in each direction, the new error norm should be smaller and is denoted by $\epsilon_m(t)$. Then the order of accuracy n is estimated as

$$n(t) = \log_m \left(\frac{\epsilon_0(t)}{\epsilon_m(t)} \right). \tag{45}$$

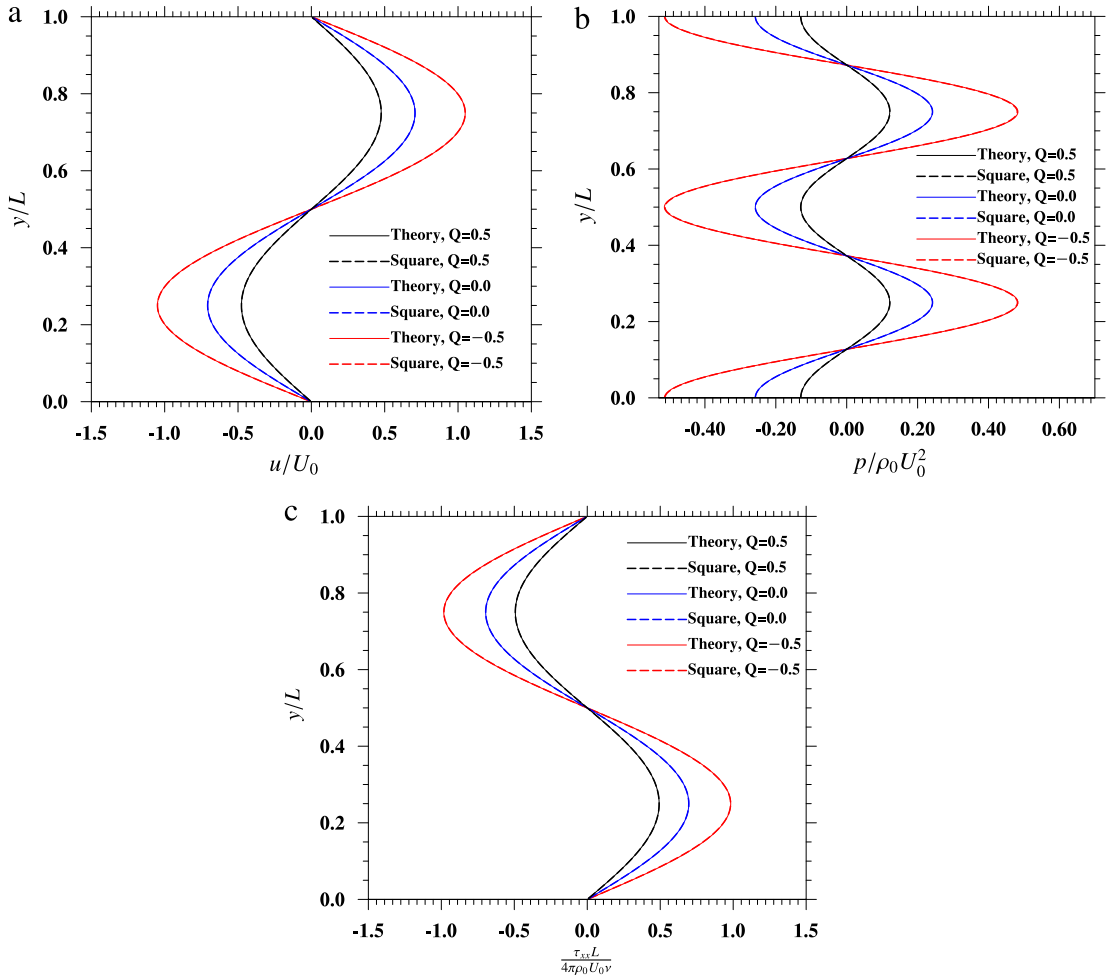

Fig. 3. Profiles of hydrodynamic variables on a vertical line: $x/L = 0.125$ at time $tU_0/L = 1.0$. Results come from case 1 in Tables 1 and 2, and the theoretical solutions given by Eq. (43). (a) Velocity in the x direction: u; (b) Pressure: p; (c) Normal stress component: τ_{xx}. All quantities are normalized as indicated. (For interpretation of the references to color in this figure legend, the reader is referred to the web version of this article.)

Table 4
The order of accuracy for the D2Q9 square-lattice model and the corresponding forcing scheme. Results are calculated at $tU_0/nx = 0.5$. The velocity **u** and normal stress τ_{xx} are examined.

$n_x \times n_y$	**u** ($L1$)	Order	**u** ($L2$)	Order	τ_{xx} ($L1$)	Order	τ_{xx} ($L2$)	Order
25 × 25	1.517E−2	(–)	1.517E−2	(–)	4.912E−3	(–)	4.894E−3	(–)
50 × 50	3.797E−3	1.998	3.797E−3	1.998	1.221E−3	2.008	1.224E−3	1.999
100 × 100	9.499E−4	1.999	9.501E−4	1.999	3.063E−4	1.995	3.064E−4	1.998
200 × 200	2.375E−4	2.000	2.376E−4	2.000	7.661E−5	1.999	7.662E−5	2.000
Averaged		1.999		1.999		2.001		1.999

The results compiled in Tables 4–6 show that the accuracy of velocity and normal stress of all three models and their corresponding forcing schemes are indeed of the second-order.

In summary, all models are perfectly consistent and their results are in excellent agreement with theoretical solutions. The forcing applied is non-uniform and time-dependent, representing the most general scenario. All models and their forcing formulation retain a second-order accuracy for the velocity and the normal stress.

5. Summary and conclusions

In this paper, the mesoscopic forcing formulation has been investigated, in its most general form, using an inverse design approach based on the multiscale Chapman–Enskog analysis. The inverse design ensures full consistency of an MRT LBM

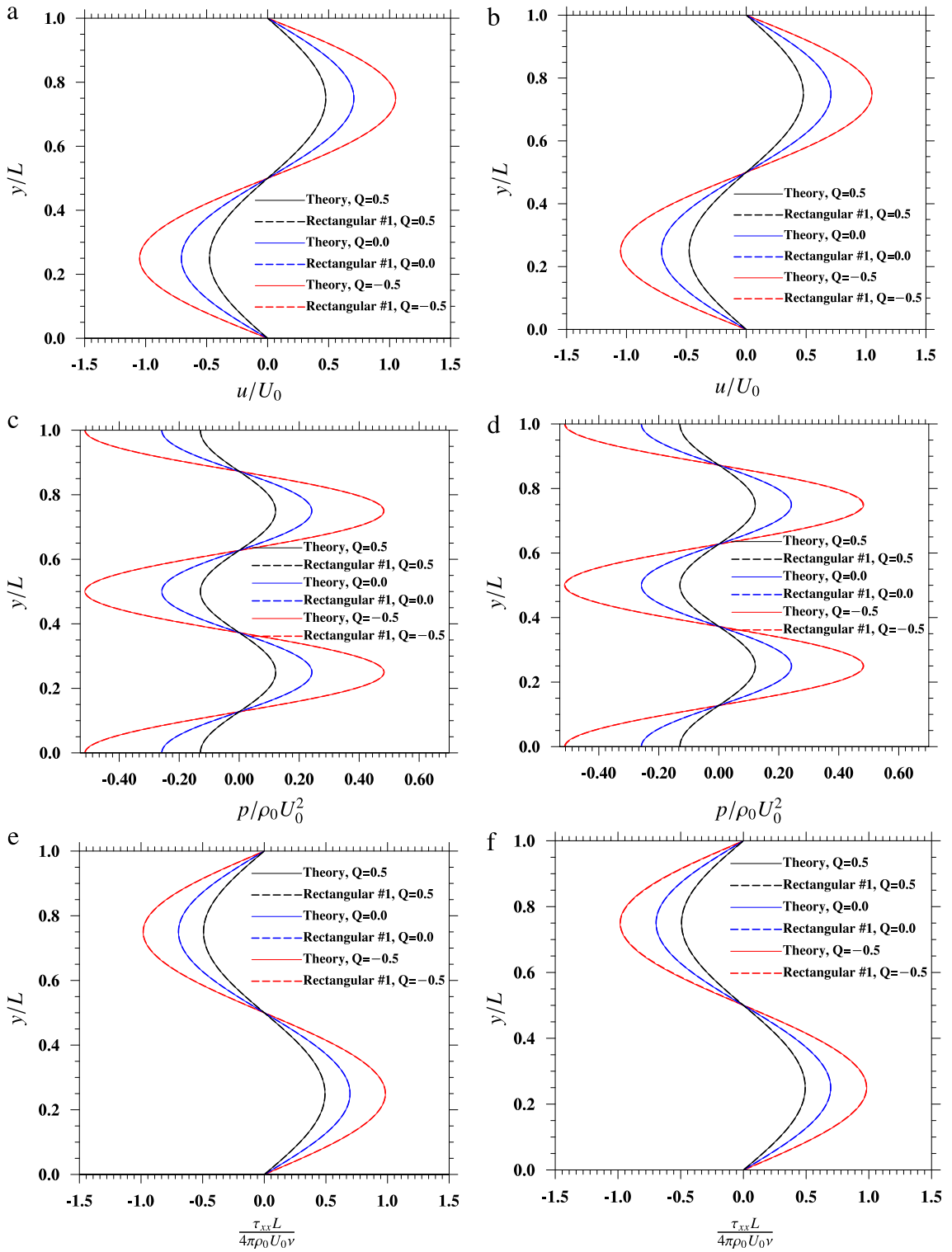

Fig. 4. Profiles of hydrodynamic variables on a vertical line: $x/L = 0.125$ at time $tU_0/L = 1.0$. Results come from case 3 in Tables 1 and 2, and the theoretical solutions given by Eq. (43). (a) Velocity in the x direction: u; (c) Pressure: p; (e) Normal stress component: τ_{xx}. The corresponding results of case 5 in Tables 1 and 2 are shown in (b), (d), and (f). All quantities are normalized as indicated.

model with the macroscopic Navier–Stokes equations and macroscopic forcing, and, at the same time, provides the most design flexibility of the mesoscopic forcing.

Table 5
The order of accuracy of Zong et al.'s rectangular-lattice model and the corresponding forcing scheme. Results are calculated at $tU_0/nx = 0.5$. The velocity **u** and normal stress τ_{xx} are examined.

$n_x \times n_y$	**u** ($L1$)	Order	**u** ($L2$)	Order	τ_{xx} ($L1$)	Order	τ_{xx} ($L2$)	Order
20 × 50	4.941E−2	(–)	4.940E−2	(–)	5.701E−2	(–)	5.646E−2	(–)
40 × 100	1.220E−2	2.018	1.220E−2	2.018	1.416E−2	2.009	1.401E−2	2.011
80 × 200	3.316E−3	1.897	3.315E−3	1.880	3.523E−3	2.007	3.484E−3	2.008
160 × 400	8.256E−4	2.006	8.252E−4	2.006	8.802E−4	2.001	8.704E−4	2.001
Averaged		1.968		1.968		2.006		2.006

Table 6
The order of accuracy of Peng et al.'s rectangular-lattice model [31] and the corresponding forcing scheme. Results are calculated at $tU_0/nx = 0.5$. The velocity **u** and normal stress τ_{xx} are examined.

$n_x \times n_y$	**u** ($L1$)	Order	**u** ($L2$)	Order	τ_{xx} ($L1$)	Order	τ_{xx} ($L2$)	Order
25 × 50	2.760E−2	(–)	2.759E−2	(–)	2.846E−2	(–)	2.795E−2	(–)
50 × 100	6.465E−3	2.094	6.464E−3	2.094	7.045E−3	2.014	6.947E−2	2.008
100 × 200	1.411E−3	2.196	1.411E−3	2.196	1.784E−3	1.981	1.758E−3	1.982
200 × 400	3.132E−4	2.172	3.131E−4	2.172	4.513E−4	1.983	4.448E−4	1.983
Averaged		2.154		2.154		1.993		1.991

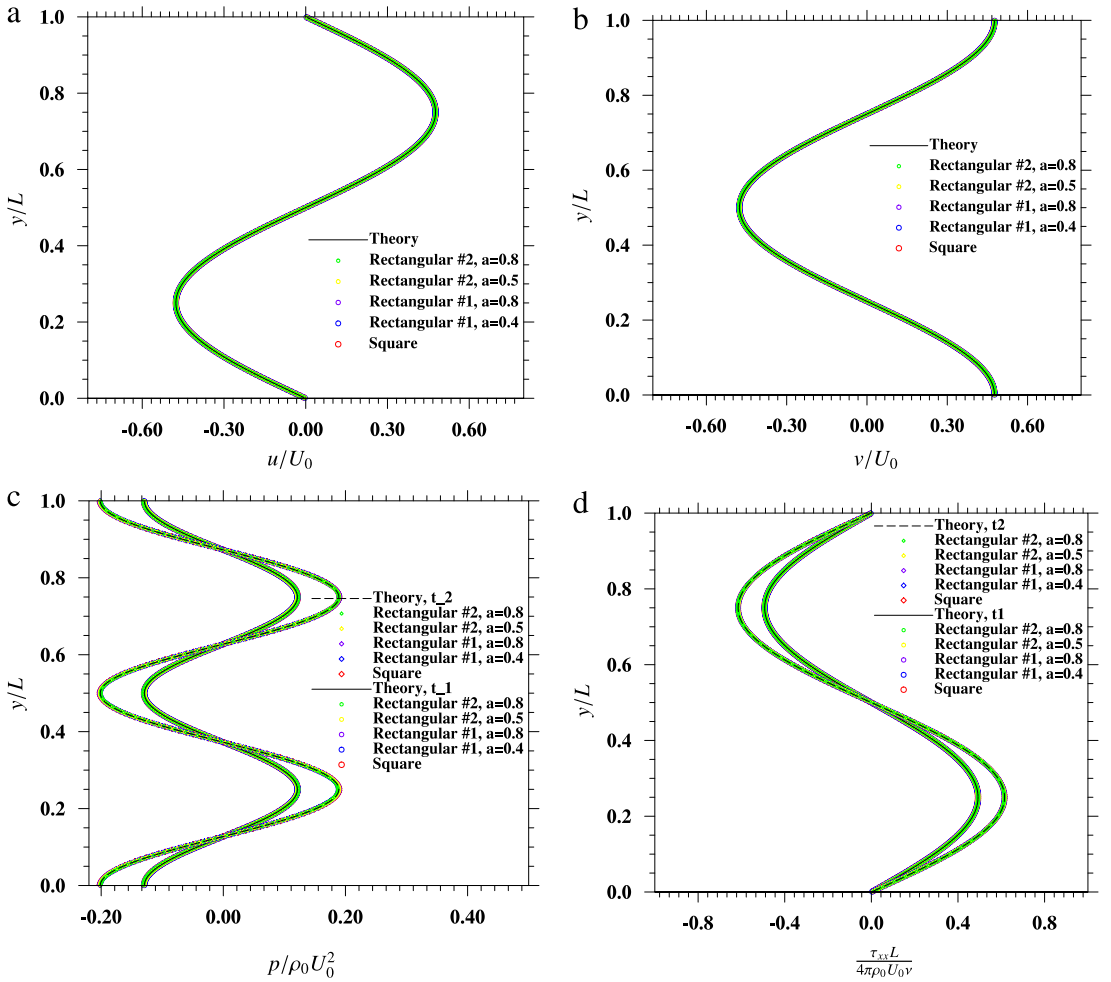

Fig. 5. Comparison of profiles on a vertical line at $x/L = 0.125$. Results of all cases from Tables 1 and 2 and the theoretical results given by Eq. (43) are compared here. (a) Velocity in the x direction: u; (b) Velocity in the y direction: v; (c) Pressure p at two different times: $t_1U_0/L = 5/16$ and $t_2U_0/L = 7/8$; (d) τ_{xx} at two different times: $t_1U_0/L = 5/16$ and $t_2U_0/L = 7/8$. All quantities are normalized as indicated.

We first re-visited the standard D2Q9 MRT model on the square lattice, to demonstrate how the inverse design is conducted. Six elements of the 9-component mesoscopic forcing term can be determined uniquely by the consistency requirements with the hydrodynamic equations. The additional benefit is then to find out that three elements in the 9-component mesoscopic forcing term are irrelevant to the Navier–Stokes equations, can thus can be chosen for better numerical stability, an topic that can be studied in the future. In our simulations here, we simply set them to zero. For the square lattice model, we did compare our results with $\Psi_3^{(1)} = \Psi_5^{(1)} = \Psi_7^{(1)} = 0$, to numerical results based on Guo et al. [26] forcing formulation. We find that the results are identical and this comparison is not included here.

The same inverse design analysis was carried out to the two new MRT LBM models on a rectangular grid, recently developed by Zong et al. [30, Section 3] and Peng et al. [31, Appendix] with the considerations of external forcing. The final results of the forcing formulation are similar to the design for the square lattice, namely, three elements of the forcing term in each case are still free parameters.

To validate these models and the forcing formulation, we designed a 2D forced Taylor–Green vortex flow with a non-uniform and time-dependent macroscopic forcing. Both decaying and augmenting flow fields can be obtained by tuning the value of a parameter Q in the forcing term. All three models were tested with three different Q values. For the two rectangular lattice models, two grid aspect ratios were used. Both the time evolution at a given point and vertical profiles at a given time are used to validate the numerical results. In all cases, the simulations results are in excellent agreement with the analytical solutions. We stress that we also considered pressure and normal stress in the comparison (the shear stress is zero in the forced Taylor–Green vortex flow). The inverse design can be applied to D3Q19 MRT LBM model on a non-standard (*i.e.,* a cuboid) grid, which is reported in a separate paper [32].

We also confirm that, in all cases, the LBM models with the proposed formulation of mesoscopic forcing, retain the second-order accuracy in space and time.

With the general non-uniform and time-dependent forcing, one could then treat a variety of flows with external or internal forces. The inverse design analysis we introduced in this paper is straightforward and general. The inverse design process is capable of revealing all inherent links between the Navier–Stokes equations and the lattice Boltzmann equations.

Acknowledgments

This work has been supported by the US National Science Foundation (NSF) under grants CNS1513031, CBET-1235974, and AGS-1139743 and by Air Force Office of Scientific Research under grant FA9550-13-1-0213. LPW also acknowledges support from the Ministry of Education of PR China and Huazhong University of Science and Technology through Chang Jiang Scholar Visiting Professorship. The authors (HM, CP and LPW) would like to acknowledge the travel support from US National Science Foundation (NSF) to attend ICMMES-2015, held in CSRC (www.csrc.ac.cn), Beijing, July 20–24, 2015, under the Grant CBET-1549614. Computing resources are provided by National Center for Atmospheric Research through CISL-P35751014, and CISL-UDEL0001 and by University of Delaware through NSF CRI 0958512.

Appendix

In this section, the forcing scheme based on Peng et al.'s [31] rectangular-lattice model will be provided. Peng et al.'s model uses the identical transformation matrix $\mathbf{M}$ from Bouzidi et al. [34], given as

$$\mathbf{M} = \begin{bmatrix} 1 & 1 & 1 & 1 & 1 & 1 & 1 & 1 & 1 \\ -2r_1 & r_5 & r_6 & r_5 & r_6 & r_1 & r_1 & r_1 & r_1 \\ 4 & -2 & -2 & -2 & -2 & 1 & 1 & 1 & 1 \\ 0 & 1 & 0 & -1 & 0 & 1 & -1 & -1 & 1 \\ 0 & -2 & 0 & 2 & 0 & 1 & -1 & -1 & 1 \\ 0 & 0 & a & 0 & -a & a & a & -a & -a \\ 0 & 0 & -2a & 0 & 2a & a & a & -a & -a \\ -2r_2 & r_7 & r_8 & r_7 & r_8 & r_2 & r_2 & r_2 & r_2 \\ 0 & 0 & 0 & 0 & 0 & 1 & -1 & 1 & -1 \end{bmatrix}, \tag{46}$$

where $r_1 = a^2 + 1$, $r_2 = a^2 - 1$, $r_5 = 1 - 2a^2$, $r_6 = a^2 - 2$, $r_7 = a^2 + 2$, and $r_8 = -2a^2 - 1$ for simplicity. The key to fulfill the isotropy condition is to introduce new degrees of freedom by extending the equilibrium moments. In order to satisfy three equalities as shown in Eq. (34), at least three degrees of freedom must be constrained. Peng et al. introduced 5 new degrees of freedom into the extended equilibrium moments, namely, the equilibrium moments are extended to take the form $\mathbf{m}^{(eq)} = \mathbf{m}^{(eq,0)} + \epsilon\mathbf{m}^{(eq,1)}$, where $\epsilon\mathbf{m}^{(eq,1)}$ includes higher-order stress components. By performing the Chapman–Enskog expansion similar to those presented in Sections 2 and 3, it is straightforward to design the elements

of $\mathbf{m}^{(eq,0)}$ and $\epsilon\mathbf{m}^{(eq,1)}$. The final formulation is

$$\mathbf{m}^{(eq)} = \mathbf{m}^{(eq,0)} + \epsilon\mathbf{m}^{(eq,1)} = \begin{bmatrix} \delta\rho \\ \delta\rho\left(6c_s^2 - 2r_1\right) + 3\rho_0\left(u^2+v^2\right) \\ \alpha\delta\rho + \beta\rho_0\left(u^2+v^2\right) \\ \rho_0 u \\ \dfrac{(\gamma-2r_2)}{a^2}\rho_0 u \\ \rho_0 v \\ \gamma\rho_0 v \\ \delta\rho\left(3r_3c_s^2 - 2r_2\right) + 3\rho_0\left(a^2u^2 - \dfrac{v^2}{a^2}\right) \\ \rho_0 uv \end{bmatrix} + \rho_0 \begin{bmatrix} 0 \\ x_1\partial_x u + x_2\partial_y v \\ 0 \\ 0 \\ 0 \\ 0 \\ 0 \\ x_3\partial_x u + x_4\partial_y v \\ x_5\left(\partial_x v + \partial_y u\right) \end{bmatrix}, \tag{47}$$

where $a = dy/dx$ is the lattice aspect ratio, $r_3 = \frac{a^4-1}{a^2}$, and $r_4 = \frac{a^4+1}{a^2}$. It is noted that the leading-order term $\mathbf{m}^{(eq,0)}$ (the first part on the right hand side of Eq. (47)) is identical to Eq. (38) with $\theta = 0$, and the additional part $\epsilon\mathbf{m}^{(eq,1)}$ contains 5 parameters, x_1 to x_5. c_s is the speed of sound in LBM unit. γ is the coefficient of equilibrium moment $q_y^{(eq,0)}$ and it has the same definition as what is defined in Section 2 for the square lattice model, and in Section 3 for Zong's model. In the square lattice model, γ has to be -1, as indicated by Eqs. (25) and (26c). However, γ is a free parameter in both rectangular lattice models. The additional part of equilibrium moments $\epsilon\mathbf{m}^{(eq,1)}$ are functions of normal velocity gradients, shear velocity gradients and a few coefficients: $x_i,\ (i = 1,\ 2,\ \ldots, 5)$. These coefficients are determined as

$$x_1 = s_e^*\left(5 - 6c_s^2 + \gamma\right) - 6\nu^V, \tag{48a}$$

$$x_2 = s_e^*\left(2 - 6c_s^2 + \gamma + 3a^2\right) - 6\nu^V, \tag{48b}$$

$$x_3 = s_n^*\left(3a^2 - \frac{\gamma+2}{a^2} - 3r_3c_s^2\right) - 3r_3\nu^V - 3r_4\nu, \tag{48c}$$

$$x_4 = s_n^*\left[a^2(\gamma+2) - 3 - 3r_3c_s^2\right] - 3r_3\nu^V + 3r_4\nu, \tag{48d}$$

$$x_5 = s_c^*\frac{\gamma+2}{3} - \nu, \tag{48e}$$

where $s_e^* = \delta_t(2-s_e)/(2s_e)$, $s_n^* = \delta_t(2-s_n)/(2s_n)$, and $s_c^* = \delta_t(2-s_c)/(2s_c)$. Other parameters are defined in Sections 2 and 3.

According to the lattice Boltzmann equation, Eq. (1), the equilibrium moments should be calculated in the collision step so we must calculate the additional part $\epsilon\mathbf{m}^{(eq,1)}$ every time step. The coefficients in $\mathbf{m}^{(eq,1)}$ (x_1 to x_5) are constant so they only need to be calculated once. However, the normal velocity gradients and the strain rate should be updated every time step according to the formulae derived in [31]:

$$\partial_x u = \frac{c_4 s_e \epsilon m_2^{(1)} - c_2 s_n \epsilon m_8^{(1)}}{(c_1c_4 - c_2c_3)\,\rho_0\delta_t}, \tag{49a}$$

$$\partial_y v = \frac{c_3 s_e \epsilon m_2^{(1)} - c_1 s_n \epsilon m_8^{(1)}}{(c_2c_3 - c_1c_4)\,\rho_0\delta_t}, \tag{49b}$$

$$s_{ij} = \frac{1}{2}\left(\partial_x v + \partial_y u\right) = \frac{s_c \epsilon m_9^{(1)}}{2\rho_0\delta_t c_5}, \tag{49c}$$

where $\epsilon m_i^{(1)} = m_i - m_i^{(0)} = m - m_i^{(0,eq)}$, and

$$c_1 = \left(\frac{s_e x_1}{\delta_t} - 5 + 6c_s^2 - \gamma\right), \tag{50a}$$

$$c_2 = \left(\frac{s_e x_2}{\delta_t} - 3a^2 - \gamma + 6c_s^2 - 2\right), \tag{50b}$$

$$c_3 = \left[\frac{s_n x_3}{\delta_t} - 3a^2 + \frac{(\gamma+2)}{a^2} + 3r_3c_s^2\right], \tag{50c}$$

$$c_4 = \left[\frac{s_n x_4}{\delta_t} - \frac{(\gamma+4)\,a^2}{a} + 3r_3c_s^2 + 3\right], \tag{50d}$$

$$c_5 = \left[\frac{s_c x_5}{\delta_t} - \frac{(\gamma+2)}{3}\right]. \tag{50e}$$

The expression of bulk and shear viscosity in this model could be derived from Eqs. (48a) and (48e), respectively,

$$\nu^V = \frac{1}{6}\left[s_e^*\left(5 - 6c_s^2 + \gamma\right) - x_1\right], \tag{51a}$$

$$\nu = s_c^* \frac{\gamma + 2}{3} - x_5. \tag{51b}$$

Thus, it is clear that x_1 and x_5 could be used to adjust bulk and shear viscosity, respectively. In this manner, the relaxation times s_e and s_c are no longer constrained by the value of viscosity. This feature could provides extra flexibility that can be used to adjust fluid viscosity [36], treat non-Newtonian fluid flows [37], or to improve numerical stability. In this paper, we simply set x_1 and x_5 to zero. On the other hand, x_2, x_3, x_4 are used to restore the isotropy property of viscosity, namely, they are implemented to achieve the relationships indicated by Eq. (34).

Finally, the mesoscopic forcing scheme derived by the inverse design for this model is

$$\mathbf{\Psi} = \begin{bmatrix} 0 \\ 6\left(1 - 0.5s_e\right)\left(uF_x + vF_y\right) \\ \Psi_3 \\ \left(1 - 0.5s_j\right)F_x \\ \Psi_5 \\ \left(1 - 0.5s_j\right)F_y \\ \Psi_7 \\ 6(1 - 0.5s_n)\left(a^2uF_x - vF_y/a^2\right) \\ (1 - 0.5s_c)\left(vF_x + uF_y\right) \end{bmatrix}. \tag{52}$$

Once again, three (Ψ_3, Ψ_5, Ψ_7) of the 9 components are *unspecified* or free, meaning that their values do not affect the hydrodynamic equations. Eq. (52) is simply the special form of Eq. (37) with $\theta = 0$. In summary, all results derive from Peng et al.'s rectangular-lattice model [31] are similar and theoretically consistent with the results from the other two models discussed in Sections 2 and 3.

Again, the expressions of normal stress and shear stress should incorporate the effect of forcing and they are modified as

$$\tau_{xx} = -\tau_{yy} = \frac{\left(a^4 - 1\right)\left[\left(1 - 0.5s_e\right)\epsilon m_2^{(1)} + 0.5\delta_t\Psi_2\right] - 2a^2\left[\left(1 - 0.5s_n\right)\epsilon m_8^{(1)} + 0.5\delta_t\Psi_8\right]}{6\left(a^4 + 1\right)}, \tag{53a}$$

$$\tau_{xy} = -\left(1 - 0.5s_c\right)\epsilon m_9^{(1)} - 0.5\delta_t\Psi_9, \tag{53b}$$

where $\epsilon m_2^{(1)}$, $\epsilon m_8^{(1)}$ and $\epsilon m_9^{(1)}$ are calculated according to $\epsilon\mathbf{m}^{(1)} = -\mathbf{m}^{(0)} = \mathbf{Mf} - \mathbf{m}^{(0)}$, and $\mathbf{m}^{(0)} = \mathbf{m}^{(eq,0)}$ is provided by Eq. (47). Ψ_2, Ψ_8 and Ψ_9 should be calculated based on Eq. (52). Thus, the effect of forcing is included when calculating the normal stress and shear stress (or strain-rate components). Once again, Eq. (53) is simply the special form of Eq. (39) with $\theta = 0$.

References

[1] X. He, L.-S. Luo, A priori derivation of the lattice Boltzmann equation, Phys. Rev. E 55 (1997) R6333.
[2] X. He, L.-S. Luo, Theory of the lattice Boltzmann method: From the Boltzmann equation to the lattice Boltzmann equation, Phys. Rev. E 56 (1997) 6811.
[3] Y.H. Qian, D. d'Humieres, P. Lallemand, Lattice BGK models for NavierStokes equation, Europhys. Lett. 17 (1992) 479–484.
[4] P. Lallemand, L.-S. Luo, Theory of the lattice Boltzmann method: Dispersion, dissipation, isotropy, Galilean invariance, and stability, Phys. Rev. E 61 (2000) 6546.
[5] L.-S. Luo, et al., Numerics of the lattice Boltzmann method: Effects of collision models on the lattice Boltzmann simulations, Phys. Rev. E 83 (2011) 056710.
[6] L.-P. Wang, O. Ayala, H. Gao, et al., Study of forced turbulence and its modulation by finite-size solid particles using the lattice Boltzmann approach, Comput. Math. Appl. 67 (2014) 363–380.
[7] H. Gao, H. Li, L.-P. Wang, Lattice Boltzmann simulation of turbulent flow laden with finite-size particles, Comput. Math. Appl. 65 (2013) 194–210.
[8] P. Lallemand, L.-S. Luo, Lattice Boltzmann method for moving boundaries, J. Comput. Phys. 184 (2003) 406–421.
[9] S. Chen, G. Doolen, Lattice Boltzmann method for fluid flows, Annu. Rev. Fluid Mech. 8 (1998) 2527.
[10] S. Succi, I. Karlin, H. Chen, Colloquium: Role of the H theorem in lattice Boltzmann hydrodynamic simulations, Rev. Modern Phys. 74 (2002) 1203.
[11] D. Yu, R. Mei, L.-S. Luo, W. Shyy, Viscous flow computations with the method of lattice Boltzmann equation, Prog. Aerosp. Sci. 39 (2003) 329.
[12] L.-P. Wang, B. Afsharpoya, Modeling fluid flow in fuel cells using the lattice Boltzmann approach, Math. Comput. Simul. 72 (2006) 242–248.
[13] H. Gao, C.Q. Qiu, D. Fan, Y. Jin, L.-P. Wang, Three-dimensional microscale flow simulation and colloid transport modeling in saturated soil porous media, Comput. Math. Appl. 59 (2010) 2271–2289.
[14] Peng, et al., Implementation issues and benchmarking of lattice Boltzmann method for moving particle simulations in a viscous flow, Comput. Math. Appl. (2015) http://dx.doi.org/10.1016/j.camwa.2015.08.027.
[15] Z.-H. Chai, T.-S. Zhao, Effect of the forcing term in the multiple-relaxation-time lattice Boltzmann equation on the shear stress or the strain rate tensor, Phys. Rev. E 86 (2012) 016705.
[16] M. Junk, W.-A. Yong, Rigorous Navier–Stokes limit of the lattice Boltzmann equation, Asymptot. Anal. 35 (2003) 165–185.
[17] M. Junk, A. Klar, L.-S. Luo, Asymptotic analysis of the lattice Boltzmann equation, J. Comput. Phys. 210 (2005) 676–704.
[18] Z. Yang, W.-A. Yong, Asymptotic analysis of the lattice Boltzmann method for generalized newtonian fluid flows, Multiscale Model. Simul. 12 (2014) 1028.
[19] W.-A. Yong, W. Zhao, L.-S. Luo, Theory of the lattice Boltzmann method: Derivation of macroscopic equations via the Maxwell iteration, Phys. Rev. E 93 (2016) 033310.

[20] X. He, Q. Zou, L.-S. Luo, Analytic solutions of simple flows and analysis of nonslip boundary conditions for the lattice Boltzmann BGK model, J. Stat. Phys. 87 (1997) 115.
[21] L.-S. Luo, Unified theory of lattice Boltzmann models for nonideal gases, Phys. Rev. Lett. 81 (8) (1998) 1618–1621.
[22] L.-S. Luo, Theory of the lattice Boltzmann method: Lattice Boltzmann models for nonideal gases, Phys. Rev. E 62 (4) (2000) 4982–4996.
[23] N.S. Martys, X. Shan, H. Chen, Evaluation of the external force term in the discrete Boltzmann equation, Phys. Rev. E 58 (1998) 6855.
[24] A.J.C. Ladd, R. Verberg, Lattice-Boltzmann simulations of particle–fluid suspensions, J. Stat. Phys. 104 (2001) 1191.
[25] J.M. Buick, C.A. Greated, Gravity in a lattice Boltzmann model, Phys. Rev. E 61 (2000) 5307.
[26] Z. Guo, C. Zheng, B. Shi, Discrete lattice effects on the forcing term in the lattice Boltzmann method, Phys. Rev. E 65 (046308) (2002) 1–6.
[27] A.A. Mohamad, A. Kuzmin, A critical evaluation of force term in lattice Boltzmann method, natural convection problem, Int. J. Heat Mass Transfer 53 (2010) 990–996.
[28] S. Farnoush, M.T. Manzari, An investigation on the body force modeling in a lattice Boltzmann BGK simulation of generalized Newtonian fluids, Physica A 415 (2014) 315–332.
[29] K.N. Premnath, M.J. Pattison, S. Banerjee, Generalized lattice Boltzmann equation with forcing term for computation of wall-bounded turbulent flows, Phys. Rev. E 79 (2009) 026703.
[30] Y. Zong, C. Peng, Z. Guo, et al., Designing correct fluid hydrodynamics on a rectangular grid using MRT lattice Boltzmann approach, Comput. Math. Appl. (2015) http://dx.doi.org/10.1016/j.camwa.2015.05.021.
[31] C. Peng, H.D. Min, Z.L. Guo, L.-P. Wang, A correct lattice Boltzmann model on a 2D rectangular grid, J. Comput. Phys. (2016) submitted for publication.
[32] L.-P. Wang, H.D. Min, C. Peng, N. Geneva, Z.L. Guo, A lattice-Boltzmann scheme of the Navier–Stokes equation on a 3D cuboid lattice, Comput. Math. Appl. (2016) submitted for publication.
[33] X. He, L.-S. Luo, Lattice Boltzmann Model for the Incompressible Navier–Stokes Equation, J. Stat. Phys. 88 (1997) 927944.
[34] M. Bouzidi, D. dHumi'eres, P. Lallemand, et al., Lattice Boltzmann equation on a two-dimensional rectangular grid, J. Comput. Phys. 172 (2001) 704–717.
[35] J. Zhou, MRT rectangular lattice Boltzmann method, Internat. J. Modern Phys. C 23 (5) (2012) 1250040.
[36] T. Inamuro, A lattice kinetic scheme for incompressible viscous flows with heat transfer, Philos. Trans. R. Soc. Lond. A Math. Phys. Eng. Sci. 360 (2002) 477–484.
[37] L. Wang, J. Mi, X. Meng, et al., A localized mass-conserving lattice Boltzmann approach for non-Newtonian fluid flows, Commun. Comput. Phys. (2014) http://dx.doi.org/10.4208/cicp.2014.m303.